

A Heteroclinic Connection between Two Saddle Slow Manifolds in the Olsen Model

Elle Musoke, Bernd Krauskopf, and Hinke M. Osinga

Department of Mathematics, University of Auckland, Private Bag 92019

Auckland, 1142, New Zealand

elle.musoke@auckland.ac.nz

Received (to be inserted by publisher)

The abstract should summarize the context, content and conclusions of the paper. It should not contain any references or displayed equations. Typeset the abstract in 10 pt Times Roman with baselineskip of 12 pt, making an indentation of 1.6 cm on the left and right margins.

Keywords: A list of 3–5 keywords are to be supplied.

1. Introduction

Multiple-time scale dynamical systems are characterized by certain variables evolving on a fast time scale while other variables evolve on a slower time scale. The separation of variables into fast and slow can be found in many systems: chemical systems, neurons, electric circuits, lasers, and predator-prey dynamics, among others, have been described by slow-fast models [Brøns & Bar-Eli, 1991; De Maesschalck & Wechselberger, 2015; Van der Pol, 1927; Otto *et al.*, 2012; Piltz *et al.*, 2017]. In [Brøns & Bar-Eli, 1991], oscillations in the Belousov-Zhabotinsky reaction arise as a consequence of time-scale splitting. Slow-fast models for neurons are studied in [De Maesschalck & Wechselberger, 2015] in which different time scales result in neural excitability. One of the most famous slow-fast systems is presented in [Van der Pol, 1927] in which time-scale splitting again causes oscillations in a circuit. Lasers can also be modelled with slow-fast systems as shown in [Otto *et al.*, 2012] which investigated interspike interval length. A more ecological example can be found in [Piltz *et al.*, 2017] which uses a slow-fast model to investigate the effect of a changing predator diet on predator-prey dynamics. By reason of their ubiquity, various phenomena that arise from the multiple-time-scale nature of slow-fast systems are of significant interest. These have been described for two- and three-dimensional systems by well-established theory [Benoît *et al.*, 1981; Benoît, 1982, 1985; Guckenheimer, 1985; Brøns *et al.*, 2006; Krupa *et al.*, 2008].

We are concerned here with mechanisms responsible for the oscillatory behaviours exhibited by many slow-fast systems. In two-dimensional systems canard explosions, small-amplitude limit cycles transitioning to larger-amplitude relaxation oscillations were studied, for example, in the Van der Pol oscillator and the FitzHugh–Nagumo model [Benoît *et al.*, 1981; FitzHugh, 1955]. In three-dimensional systems, periodic orbits (POs) with epochs of localized small-amplitude oscillations (SAOs) and epochs of large-amplitude oscillations (LAOs) have been observed [Hudson *et al.*, 1979]. The mechanisms that cause SAOs of these appropriately named mixed-mode oscillations (MMOs) are described in [Desroches *et al.*, 2012] for three-dimensional systems. In this paper, we investigate novel phenomena that arise in four-dimensional slow-fast systems which may provide insight into undiscovered mechanisms for MMOs in higher-dimensional systems.

Previous studies exploring the mechanisms for MMOs in slow-fast dynamical systems investigate the role of so-called slow manifolds in the MMOs' generation and organisation [Vo *et al.*, 2013a,b; Harvey *et al.*, 2010; Mitry *et al.*, 2013; Hasan *et al.*, 2018]. Slow manifolds are families of trajectories on which the flow evolves on the slow timescale. A slow manifold may have families of trajectories that converge toward it in forward or backward time, respectively called the stable and unstable manifolds of the slow manifold. Slow manifolds may have both a stable and an unstable manifold in which case we say it is a saddle slow manifold.

Literature concerning slow manifolds explores slow manifolds and systems of, respectively, varying dimensions. Endocrine pituitary cells were studied with a four-dimensional slow-fast model that had a two-dimensional slow manifold in [Vo *et al.*, 2013b]. In [Harvey *et al.*, 2010] a three-dimensional slow manifold was studied in a four-dimensional model for calcium oscillations inside cells. In [Vo *et al.*, 2013a] a four-dimensional model for a pituitary lactotrophic cell was investigated from both a two- and three-timescale viewpoints. From the two-timescale perspective, the model has a three-dimensional slow manifold. In [Mitry *et al.*, 2013] a six-dimensional model for an excitable neuron was investigated. The model had a two-dimensional slow manifold which plays a role in the generation of oscillations in the system. A five-dimensional model with a one-dimensional slow manifold was also investigated. In [Farjami *et al.*, 2018] techniques were developed to compute stable and unstable manifolds of one-dimensional saddle slow manifolds in three-dimensional systems. In [Hasan *et al.*, 2018], these techniques were generalised to compute a two-dimensional saddle slow manifold and its two-dimensional stable and unstable manifolds in the four-dimensional Hodgkin–Huxley model. To our knowledge, there is no literature on the computation of three-dimensional (un)stable manifolds of one-dimensional saddle slow manifolds at this time.

We consider a prototypical four-dimensional slow-fast dynamical system that exhibits MMOs, namely an Olsen model for peroxidase-oxidase reaction. First introduced by Lars F. Olsen in 1983 [Olsen, 1983], there are currently many different versions of the Olsen model of different dimensions. We consider the Olsen model in the form from [Kuehn & Szmolyan, 2015] and earlier work. The MMO Γ in the Olsen model phase space is of particular interest because it does not seem to be generated by the mechanisms for MMOs familiar from three-dimensional systems.

The classification of variables into those that evolve on a fast time scale and those that evolve on a slow time scale is not straightforward for the Olsen model because the variables are not consistently slow or fast over all regions of phase space. In fact, the Olsen model nominally has three different time scales. We focus specifically on a parameter regime corresponding to two different time scales with three fast and one slow variables. This parameter regime also corresponds to attracting Γ and was the focus in [Desroches *et al.*, 2009]. This study reported on mechanisms for Γ after a model reduction to a three-dimensional system. Two saddle slow manifolds were computed along with their stable and unstable manifolds. These gave insight into the formation of the Olsen model MMO, as well as the cause of its particular geometry. However, because of the assumptions used to reduce the model to a three-dimensional system, the dimensions of the stable manifold of one slow manifold and unstable manifold of the other were reduced to two in contrast to the corresponding three-dimensional manifolds in the full system.

Examples of computing and visualising three-dimensional manifolds are in [Waalkens *et al.*, 2005; H\'aro & de la Liave, 2006; Jorba & Olmedo, 2009]. None of these examples are in the context of computing (un)stable manifolds of saddle slow manifolds. Tools to implement the computation of three-dimensional manifolds are not widely used at this time and, once computed, it is difficult to see the dynamics on the manifold in lower-dimensional projections. Due to the nature of the current computation tools available, computing the entire three-dimensional manifold would also be computationally expensive compared to the computation of two-dimensional manifolds.

In the full system, the three-dimensional stable manifold of one slow manifold and the three-dimensional unstable manifold of the other are expected to intersect generically in a two-dimensional surface of connections between the two slow manifolds. Such a surface does not generically exist in four-dimensional systems for slow manifolds of dimension greater than one. The surface of connections also does not exist generically in systems of dimension lower than four. In these cases, the stable and unstable manifolds of the saddle slow manifolds are limited to dimensions of two or lower and therefore do not typically have robust intersections of dimension two or higher. In this research, we generalise the techniques in [Farjami

[*et al.*, 2018] with the aim of computing the three-dimensional stable and unstable manifolds of the one-dimensional saddle slow manifolds in the Olsen model. Furthermore, we use our techniques in conjunction with Lin’s method to compute the intersection of the three-dimensional stable and unstable manifolds in the full four-dimensional model. This intersection is involved in the formation and organisation of Γ and could lead to insights about the formation and organisation of MMOs in other higher-dimensional systems.

This paper is organized as follows. In the next section we give the necessary background from geometric singular perturbation theory (GPST) for defining the three-dimensional manifolds which are the focus of this research. Section 3 gives definitions of the manifolds which are then computed. In section 4, a computation of the intersection of the manifolds from section 3 is described for the case where the time-scaling parameter is greater than zero as well as for the case when the time-scaling parameter is equal to zero. Section 5 gives an analysis of differences between the manifolds computed in section 4. Conclusions are given in section 6.

2. The Olsen Model

We consider the scaled system from [Kuehn & Szmolyan, 2015], given as the system of ordinary differential equations

$$\begin{cases} \frac{dA}{dt} = \mu - \alpha A - ABY, \\ \frac{dB}{dt} = \varepsilon(1 - BX - ABY), \\ \frac{dX}{dt} = \lambda(BX - X^2 + 3ABY - \zeta X + \delta), \\ \frac{dY}{dt} = \kappa\lambda(X^2 - Y - ABY), \end{cases} \quad (1)$$

where $(A, B, X, Y) \in \mathbb{R}^4$ are positive concentrations of chemicals. The system parameters are represented by the Greek letters appearing in (1) and these have the values given in Table 1. With the minor modification, for notational convenience, of using ε for ε_b and $\frac{1}{\lambda}$ for ε^2 , they are chosen to be as in [Kuehn & Szmolyan, 2015]. The time-scaling parameters ε and λ are chosen so that we are dealing with a regime with three fast variables, A , X , and Y , and one slow variable, B .

Table 1. Parameters of system (1) as in [Kuehn & Szmolyan, 2015] so that A , X , and Y are fast and B is slow.

α	δ	ε	λ	κ	μ	ζ
0.0912	1.2121×10^{-4}	0.0037	18.5281	3.7963	0.9697	0.9847

The classical analysis of slow-fast systems considers the two singular limits, for example, [Desroches *et al.*, 2012]. In the limit of $\varepsilon = 0$, system (1) reduces to

$$\begin{cases} \frac{dA}{dt} = \mu - \alpha A - ABY, \\ \frac{dX}{dt} = \lambda(BX - X^2 + 3ABY - \zeta X + \delta), \\ \frac{dY}{dt} = \kappa\lambda(X^2 - Y - ABY), \end{cases} \quad (2)$$

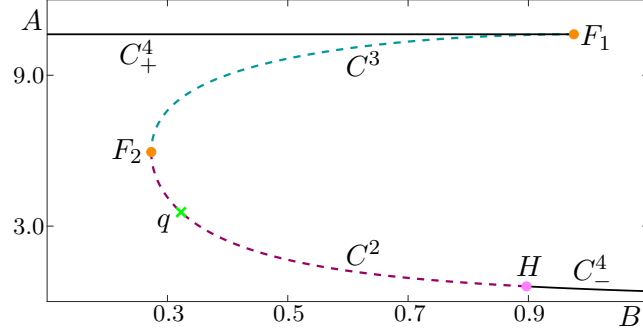


Fig. 1. Physically relevant branches C^2 , C^3 , C_{\pm}^4 of the critical manifold of (1) shown in projection onto the (B, A) -plane. Branches C^2 (dashed, raspberry curve) and C^3 (dashed, teal curve) consist of saddles of (2) and C_{\pm}^4 (solid, black curve) consist of attractors of (2). Superscripts indicate the dimension of the stable eigenspace of the branch and subscripts are used to distinguish between the two branches of attractors. Branches are divided by saddle-node bifurcation points F_1 and F_2 (orange dots) and a Hopf point H (pink dot). Also shown is a saddle equilibrium q (green cross) of (1) existing on C^2 . Parameters are as in Table 1.

with $\frac{dB}{dt} = 0$, meaning that B is a parameter of (2). We refer to the three-dimensional system (2) as the fast subsystem. Performing the time rescaling $\tau = \varepsilon t$ and then considering the limit of $\varepsilon = 0$, system (1) reduces to the differential algebraic reduced system

$$\begin{cases} 0 &= \mu - \alpha A - ABY, \\ \frac{dB}{d\tau} &= (1 - BX - ABY), \\ 0 &= \lambda(BX - X^2 + 3ABY - \zeta X + \delta), \\ 0 &= \kappa\lambda(X^2 - Y - ABY). \end{cases} \quad (3)$$

The three algebraic equations in system (3) define a one-dimensional manifold, called the critical manifold, denoted C .

The critical manifold C consists of equilibria of the fast subsystem (2), which exist in (A, B, X, Y) -space for different values of B . Their stability can be determined from the eigenvalues of the 3×3 Jacobian matrix of (2) evaluated at each point on the critical manifold. Points $p \in C$ at which the Jacobian of (2) has eigenvalues with non-zero real parts are called hyperbolic. The eigenvectors associated with the eigenvalues are categorized based on the sign of the real part of the associated eigenvalue. Eigenvectors whose associated eigenvalues have negative real parts are called stable directions of p and these span the stable eigenspace $E^s(p)$ of p . The unstable directions and the unstable eigenspace, $E^u(p)$, can be defined similarly by the eigenvectors associated with eigenvalues having positive real part. Note that the dimensions of the stable and unstable eigenspaces are equal to the number of eigenvalues with negative and positive real parts respectively. Equilibria at which the Jacobian has eigenvalues with zero real-part are called non-hyperbolic and these correspond to bifurcations of system (2) [Kuznetsov, 2009].

The critical manifold C in (A, B, X, Y) -space is divided into branches by bifurcation points of the fast subsystem (2), so that points on each branch have the same dimensions of stable and unstable eigenspaces. In other words, the branches of C are one-parameter families in B of hyperbolic equilibria of system (2). We define the stable eigenspace $E^s(C^i)$ of a branch C^i as the collection of stable eigenspaces of all the points on the branch. The dimension of $E^s(C^i)$, hence, one plus than the dimension of the stable eigenspace of each point on the branch. In our notation for branches, superscripts indicate the dimension in (A, B, X, Y) -space of the stable eigenspace of the branch. Further, we use subscripts to distinguish the two branches on which equilibria have three-dimensional stable eigenspaces, that is, are attracting.

Four branches of C lie in the physically relevant region where all phase-space variables are positive,

these are shown in Figure 1 in projection onto the (B, A) -plane. The uppermost branch denoted C_+^4 (solid, black curve) consists of stable equilibria of (2). It is separated from the branch of saddle equilibria denoted C^3 (dashed, teal curve), by a very sharp fold at the point F_1 (orange dot) at $B \approx 0.956$. Folds of the critical manifold correspond to saddle-node bifurcations of system (2) with respect to the parameter B , these are points at which one of the real eigenvalues of the Jacobian evaluated at the point changes signs. Another fold at $B \approx 0.273$ denoted F_2 (orange dot), separates C^3 from a lower branch of saddle equilibria denoted C^2 (dashed, raspberry curve). The branch C^2 ends at a Hopf bifurcation H (pink dot) at $B \approx 0.897$, where two complex-conjugate eigenvalues of the Jacobian pass through the imaginary axis of the complex plane. To the right of H , there is again a stable branch of equilibria denoted C_-^4 (solid, black curve).

The point q (green cross) on C^2 at $B \approx 0.323$ is an equilibrium of system (3) and is, hence, an equilibrium for the full system (1). The equilibrium q has a two-dimensional stable and two-dimensional unstable manifold, denoted $W^s(q)$ and $W^u(q)$, respectively. The manifolds $W^s(q)$ and $W^u(q)$ consist of trajectories in (A, B, X, Y) -space that converge to q in forward and backward time respectively. To the right of $W^u(q)$, in the (B, A) -projection, the flow is from right to left near C^2 . To the left of $W^u(q)$, in the (B, A) -projection, the flow is from left to right near C^2 . The manifolds $W^s(q)$ and $W^u(q)$ can be computed with the methods in [Krauskopf *et al.*, 2007]; They are not depicted in Figure 1, but are shown in Figure 10.

Our interest is in the branches C^3 and C^2 because they are saddle objects of different type and are crucial for organising the phase space. These branches of the critical manifold are invariant for $\varepsilon = 0$, but not for $\varepsilon > 0$. However, they do persist as locally invariant manifolds called slow manifolds [Fenichel, 1979]. The associated slow manifolds are traditionally denoted S_ε^3 and S_ε^2 but, for notational convenience, we drop the subscript indicating dependence on ε and refer to these slow manifolds for $\varepsilon > 0$ simply as S^3 and S^2 . The slow manifold S^3 has the same dimension and stability and lies at an $O(\varepsilon)$ Hausdorff distance from C^3 . In particular, S^3 converges to C^3 as $\varepsilon \rightarrow 0$. (For a definition of Hausdorff distance see, e.g., [Rockafellar & Wets, 2009].) Orbit segments that lie on a slow manifold remain slow for $O(1)$ time with respect to the slow time scale. It follows that any trajectory that remains slow for an $O(1)$ amount of slow time can be considered (to be on) a slow manifold. However, eventually trajectories on a slow manifold may become fast. Due to their finite time nature, slow manifolds are not unique; however, any two slow manifolds lie exponentially close to each other in a suitable $O(\varepsilon)$ neighbourhood of C [Fenichel, 1979]. To select unique representatives S^3 and S^2 , we consider the slow manifold that remains slow for the longest amount of time in a specific numerical setup in section 3.

The Stable Manifold Theorem tells us that each $p \in C^3$ has a stable and an unstable manifold that are tangent to and have the same dimensions as $E^s(p)$ and $E^u(p)$, respectively. We denote the stable manifold of a point $p \in C^3$ by $W^s(p)$ and its unstable manifold by $W^u(p)$. We can then define the collection of stable manifolds for $p \in C^3$ as $W^s(C^3) = \bigcup_{p \in C^3} W^s(p)$, which is a three-dimensional manifold tangent to $E^s(C^3)$. We can similarly define the three-dimensional unstable manifold $W^u(C^2)$ of C^2 which is tangent to $E^u(C^2)$.

According to Fenichel Theory, for $\varepsilon > 0$, the manifold $W^s(C^3)$ also persists in an $O(\varepsilon)$ neighbourhood as a three-dimensional local stable manifold $W_{loc}^s(S^3)$ of S^3 . The local stable manifold $W_{loc}^s(S^3)$ consists of families of trajectories that have a fast approach to S^3 then remain close to S^3 for $O(1)$ slow time. The global stable manifold $W^s(S^3)$ can be obtained by extending $W_{loc}^s(S^3)$ backwards in time. The three-dimensional unstable manifold $W^u(S^2)$ associated with S^2 is similarly defined for backwards time. Again, due to the finite-time nature of the definitions for the three-dimensional manifolds $W^s(S^3)$ and $W^u(S^2)$, they are not unique. To select unique representatives, we consider two-parameter families of orbit segments that remain slow for the longest amount of time subject to boundary conditions described in further sections.

3. Computation of saddle slow manifolds and their (un)stable manifolds

In [Farjami *et al.*, 2018] algorithms are presented for the computation of a one-dimensional saddle slow manifold and its (un)stable manifolds in a three-dimensional system. We build on their work to define and compute unique representatives S^3 and S^2 as well as their stable and unstable manifolds, respectively.

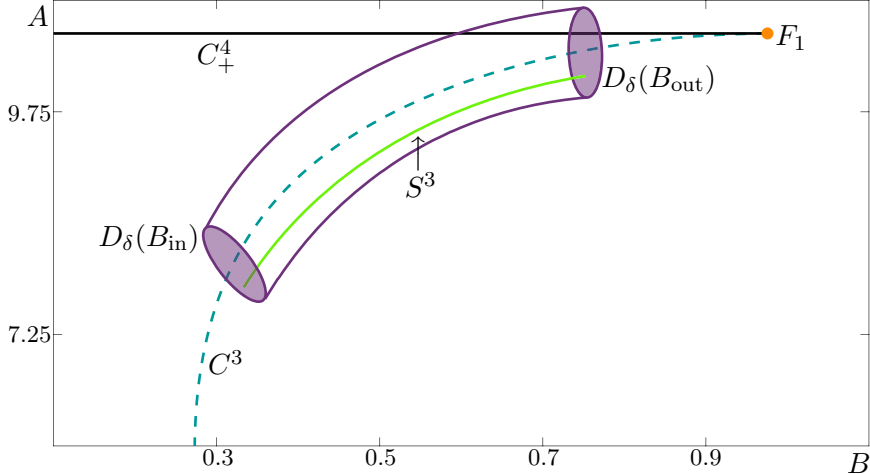


Fig. 2. A sketch of the unique representative slow manifold S^3 (green curve) projected into the (B, A) -plane. The representative slow manifold S^3 is defined by having the longest integration time while entering and exiting $D_\delta(B_{\text{in}})$ and $D_\delta(B_{\text{out}})$ (purple disks) at either end of a four-dimensional cylinder. Also shown are C^3 , C_+^4 , and F_1 .

3.1. Definition of S^3

We define the slow manifold S^3 with respect to a closed interval $[B_{\text{in}}, B_{\text{out}}]$ for the slow variable B . The values for B_{in} and B_{out} are chosen such that $[B_{\text{in}}, B_{\text{out}}] \subset (B_{F_1}, B_{F_2})$, where B_{F_1} and B_{F_2} are the B -values of the fold points F_1 and F_2 , respectively. Hence, for each $B_p \in [B_{\text{in}}, B_{\text{out}}]$ there is a unique point $p = (p_A, p_B, p_X, p_Y) \in C^3$ such that $p_B = B_p$. In the three-dimensional subsection $\{\omega \in \mathbb{R}^4 \mid \omega_B = B_p\}$ we define a solid three-sphere $D_\delta^s(B_p)$ with radius δ and centre p , given formally by

$$D_\delta^s(B_p) = \{w \in \mathbb{R}^4 \mid w_B = B_p, \|w - p\| \leq \delta\}.$$

The union

$$\mathcal{D}^s = \bigcup_{B_p \in [B_{\text{in}}, B_{\text{out}}]} D_\delta^s(B_p)$$

forms a four-dimensional compact cylinder. The superscript s indicates that The radius δ is small, but it needs to be of $O(\varepsilon)$ to ensure that S^3 lies in \mathcal{D}^s . The one-parameter family of orbit segments that enter \mathcal{D}^s via $D_\delta^s(B_{\text{in}})$ are candidates for S^3 . To select a unique representative S^3 we require that the orbit segment representing S^3 has maximal integration time in \mathcal{D}^s while satisfying appropriate boundary conditions. Our choice of boundary conditions is explained in section 3.2.

Figure 2 illustrates this definition with an enlargement of Figure 1 near the branch C^3 , where we now sketch the relevant elements of this definition. The unique representative S^3 , in projection onto the (B, A) -plane, enters \mathcal{D}^s at $D_\delta^s(B_{\text{in}})$ and exits at $D_\delta^s(B_{\text{out}})$.

3.2. Computation of $W^s(S^3)$ and S^3

Since $W^s(S^3)$ is three dimensional it is challenging to compute and difficult to visualise. In fact, $W^s(S^3)$ can be represented as a two-parameter family of orbit segments that enter \mathcal{D}^s at $D_\delta^s(B_p)$ for some $B_p \in [B_{\text{in}}, B_{\text{out}}]$, and remain inside \mathcal{D}^s for $O(1)$ slow time. A natural way forward is to consider $W^s(S^3)$ as a one-parameter family of two-dimensional submanifolds. These submanifolds can be computed by generalizing the approach in [Farjami *et al.*, 2018], which can then be implemented in the two-point boundary value problem (2PBVP) continuation package AUTO [Doedel, 2007].

Similarly to S^3 , we select and approximate a specific candidate for $W^s(S^3)$ by requiring that each orbit segment lying on $W^s(S^3)$ has maximal integration time inside \mathcal{D}^s and satisfies appropriate boundary conditions. We now turn to the computation of the three-dimensional manifold $W^s(S^3)$ in the region where

a corresponding two-dimensional stable manifold was investigated in the reduced model in [Desroches *et al.*, 2009].

To select a submanifold we first define a two-dimensional plane Σ that is transverse to the flow and to $E^u(C^3)$. We can define Σ by fixing A and either X or Y . A smooth, one-parameter family of orbit segments of (1) is then given by the property that they begin in Σ , enter \mathcal{D}^s at $D_\delta^s(B_p)$ for some $B_p \in [B_{\text{in}}, B_{\text{out}}]$, and remain inside \mathcal{D}^s for $O(1)$ slow time. We denote by W_Σ^s the collection of those parts of these orbit segments that enter \mathcal{D}^s in the fast direction. The later parts that evolve mostly in the B -direction inside \mathcal{D}^s for $O(1)$ slow time are approximate segments of S^3 . If such a later part of the orbit segment includes a fast exit from \mathcal{D}^s , the fast part lies on the unstable manifold $W^u(S^3)$ of S^3 in good approximation.

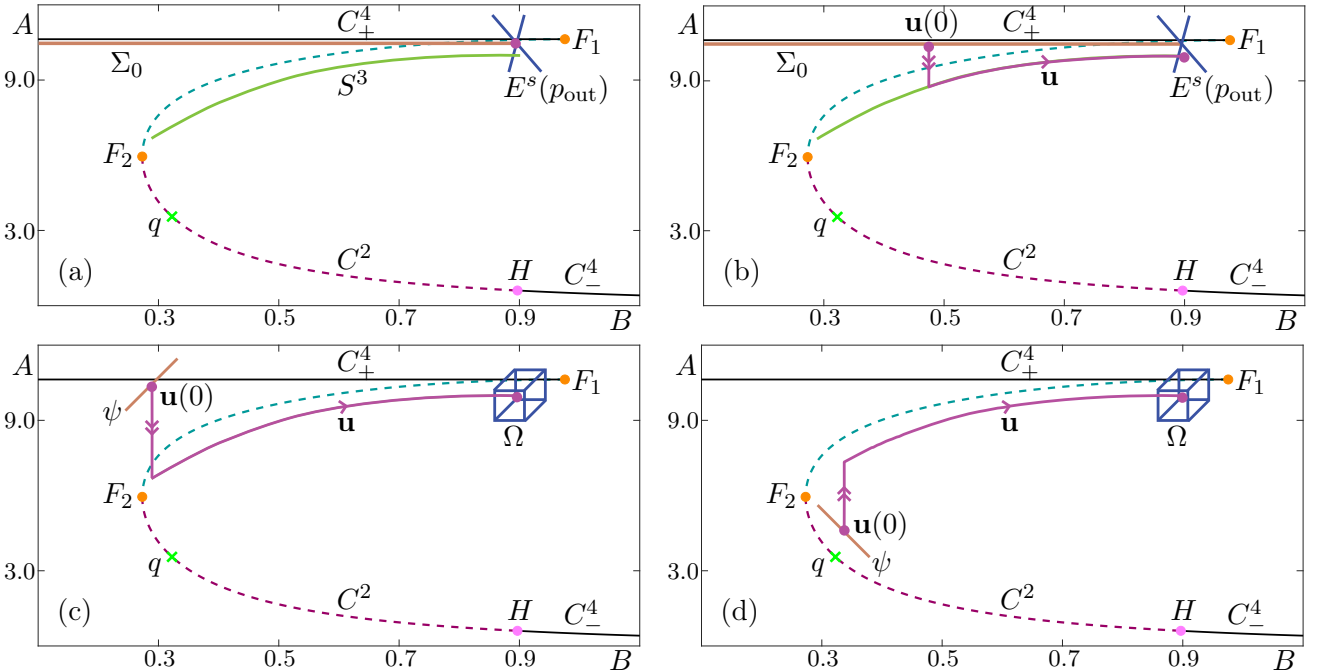


Fig. 3. A sketch in projection onto the (B, A) -plane of the numerical set-up for the computation of submanifolds of $W^s(S^3)$. Also shown are C^2 , C^3 , C_\pm^4 , F_1 , F_2 , H and q . Panel (a) shows a sketch at the start of the first homotopy step for computing $W_{\Sigma_0}^s$ with S^3 (a green curve), $E^s(p_{\text{out}})$ (blue cross), and the plane Σ_0 (mocha line) defined by the A - and Y -coordinates of the point p_{out} . Panel (b) shows a representative orbit segment \mathbf{u} (magenta curve) of the first homotopy step. Panel (c) shows an illustration of the selection of a \mathbf{u} with maximal integration time that starts at ψ (mocha line) and ends on Ω (blue cube); here the one-dimensional subset $\psi \subset \Sigma_0$ is defined by fixing $B = B_{\text{in}}$ and Ω is spanned by $E^s(p_{\text{out}})$ and a vector in the B -direction. Panel (d) is a sketch of the selection of a different submanifold W_Σ^s for Σ on the other side of the critical manifold.

We compute the submanifold W_Σ^s as a one-parameter family of orbit segments $\mathbf{u} = \{\mathbf{u}(s) \mid 0 \leq s \leq 1\}$ of the rescaled system

$$\frac{d\mathbf{u}}{ds} = TF(\mathbf{u}), \quad (4)$$

where $\mathbf{u}(s) = (A(s), B(s), X(s), Y(s)) \in \mathbb{R}^4$ is the vector of chemical concentrations, F is the right-hand side of (1) and T is the total integration time on the fast timescale. Orbit segments $\mathbf{u} \in W_\Sigma^s$ must satisfy the boundary conditions

$$\mathbf{u}(0) \in \Sigma, \quad (5)$$

$$\mathbf{u}(1) \in \Omega = E^s(p_{\text{out}}) \times [0 \ 1 \ 0 \ 0]^{tr}, \quad (6)$$

and

$$T = T^B \quad (7)$$

where, for each $B_p \in [B_{\text{in}}, B_{\text{out}}]$, T^B is the maximum integration time of an orbit segment with $\mathbf{u}(0)_B = B_p$ satisfying (5) and (6). Equations (5), (6) and (7) define four conditions on solutions of (4) so that there is a one-parameter family of solutions to this 2PBVP. Once an initial \mathbf{u} satisfying (4), (5), (6), and (7) is found, it is possible to sweep out the rest of W_Σ^s by continuing \mathbf{u} with varying $\mathbf{u}(0)_B$ and T . The challenge in this type of set-up is generally the computation of an initial orbit segment that satisfies the boundary conditions. For this purpose, we use homotopy steps as in [DesRoches *et al.*, 2009; Farjami *et al.*, 2018].

In the first homotopy step, we choose the point $p_{\text{out}} = (p_A, p_B, p_X, p_Y) \in C^3$ by fixing p_B and the section $\Sigma = \Sigma_0 = \{\omega \in \mathbb{R} \mid \omega_A = p_A, \omega_Y = p_Y\}$, and define the boundary condition

$$\mathbf{u}(1) \in E^s(p_{\text{out}}). \quad (8)$$

Then $\mathbf{u}(t) = p_{\text{out}}$ is a solution to (4), (5), and (8) with $T = 0$. In the second homotopy step, we continue the orbit segment \mathbf{u} by increasing T until $\mathbf{u}(0)_B$ is sufficiently small. We then can perform a third homotopy step to move Σ to a desired location. In a final homotopy step, we impose the condition

$$\mathbf{u}(0) \in \psi = \Sigma_0 \cap \{\omega \in \mathbb{R}^4 \mid \omega_B = B_{\text{in}}\}. \quad (9)$$

By construction the \mathbf{u} at the end of the previous homotopy step is a solution to (4), (6), and (9). Integration time T is then increased until a local maximum T_B is attained. Here, we fix $\mathbf{u}(0)_B$ to ensure that an increase in integration time is the result of the slow segment's approach to S^3 and not the result of decreasing $\mathbf{u}(0)_B$. We now have an initial \mathbf{u} satisfying (5), (6), and (7) with which we can sweep out the rest of W_Σ^s .

Figure 3 illustrates, step-by-step in projection onto the (B, A) -plane, the homotopy steps for computing W_Σ^s . Each panel shows C from Figure 1 with additional information for the computation. Figures 3(a)–(c) illustrate the set-up for obtaining a first solution on $W_{\Sigma_0}^s$ via homotopy steps. The point $p_{\text{out}} = (10.6055, 0.9, 0.0492484, 0.000230006)$ with $p_B = 0.9$ lies on C^3 and the section $\Sigma_0 = \{\omega \in \mathbb{R} \mid \omega_A = 10.6055, \omega_Y = 0.000230006\}$ intersects $E^s(p_{\text{out}})$ at the point p_{out} . We impose the condition (5), that is, we impose two restrictions on the startpoint $\mathbf{u}(0)$ of the orbit segment \mathbf{u} because Σ_0 is two dimensional. To find a unique \mathbf{u} satisfying (6) we require the more restrictive condition (8) that imposes two restrictions on $\mathbf{u}(1)$. Hence, the overall 2PBVP is well defined. Note that $E^s(p_{\text{out}})$ is transverse to $W^u(S^3)$. In Figure 3(a) Σ_0 is sketched as a mocha curve directly under C_+^4 , intersecting $E^s(p_{\text{out}})$ which is sketched as a blue cross (note that in panels (a)–(b) Σ_0 is shown slightly lower for visibility). By construction, the point p_{out} is a solution of the 2PBVP defined by (4), (5), and (8) with $T = 0$.

We then increase the total integration time while allowing the B -value of $\mathbf{u}(0)$ to decrease towards F_2 . Figure 3(b) shows an intermediate orbit segment with a fast segment followed by a slow segment along S^3 . Panel (c) shows \mathbf{u} when the continuation is stopped at $\mathbf{u}(0)_B = B_{\text{in}} = 0.275$, just before $\mathbf{u}(0)_B$ reaches the B -coordinate value of F_2 .

The orbit segment illustrated in Figure 3(c) belongs to a two-parameter family of solutions \mathbf{u} of (4) that satisfy the boundary conditions (5) and (6) for $\Sigma = \Sigma_0$. In the case where we would like to compute W_Σ^s for Σ defined by different A and Y (or X) we perform an additional homotopy step to move Σ . This can be achieved after the first homotopy step, by imposing (5) and (8) on an intermediate orbit segment while keeping T and $\mathbf{u}(0)_X$ (or $\mathbf{u}(0)_Y$) as free parameters. We continue \mathbf{u} while increasing or decreasing the A - and/or Y -values (or X -values) defining Σ until we reach the desired plane. We then also decrease $\mathbf{u}(0)_B$ and stop the continuation when $\mathbf{u}(0)_B = B_{\text{in}}$. Depending on Σ , the value of B_{in} may need to be increased to avoid Σ intersecting C . Panel (d) shows an example of a different choice of Σ defined by a smaller value of A .

Figures (c)–(d), illustrate the final homotopy step in which we find an orbit segment with maximal integration time. The three-dimensional space Ω from condition (6) is shown as a blue cube and ϕ from (9) is shown as a mocha line. Panel (c) illustrates the numerical setup for $\Sigma = \Sigma_0$ while panel (d) illustrates the numerical setup for a choice of Σ on the other side of C^3 with respect to the variable A . To define a

one-parameter family of orbit segments from those satisfying (5) and (6), we select for each $B_p \in [B_{\text{in}}, B_{\text{out}}]$ the \mathbf{u} with maximal integration time such that $\mathbf{u}(0)_B = B_p$. In other words, we select a one-parameter family of \mathbf{u} that satisfy (7). We fix $\mathbf{u}(0)_B$ to ensure an increase in integration time results from a better approximation of an orbit segment in W_Σ^s . To ensure that our 2PBVP is well defined with the extra restriction on $\mathbf{u}(0)$, we allow an extra degree of freedom for $\mathbf{u}(1)$ by requiring (6) instead of (8) so that only one restriction is imposed on $\mathbf{u}(1)$. To fix $\mathbf{u}(0)_B$, we require (9) which imposes three conditions on $\mathbf{u}(0)$ and is, hence, more restrictive than (5). We now track the solution \mathbf{u} of the 2PBVP (4), (6), and (9) as T increases, forcing $\mathbf{u}(0)$ to approach $W^s(S^3) \cap \Sigma$ and $\mathbf{u}(1)$ to approach $W^u(S^3) \cap \Omega$. When a fold in T is detected, a (local) maximum T_B of the total integration time T is attained.

The orbit segment that is obtained is the desired \mathbf{u} with maximal integration time. It is not represented in a figure because it is practically identical to the orbit segment illustrated in Figure 3(c): it begins in Σ and has a fast approach to S^3 before remaining $O(\varepsilon)$ close for $O(1)$ slow time. By definition it is an orbit segment in W_Σ^s . In addition to finding an orbit segment that approximates a solution to (4) laying on W_Σ^s , we can approximate S^3 by restricting the orbit segment further to lie entirely inside $(B_{\text{in}}, B_{\text{out}})$ to exclude fast segments.

After these homotopy steps we use (5), (6), and (7) to sweep out a one-parameter family of solutions which gives an accurate approximation of W_Σ^s . Figure 4 shows $W_{\Sigma_0}^s$ (light blue surface) in projection onto (B, A, X) -space (a) and (B, A, Y) -space (b) with Σ_0 (mint surface and line). The plane Σ_0 appears as a line in panel (b) because it is defined by constant A and Y . The view is rotated relative to earlier figures to help illustrate the geometry of this submanifold. Also shown are C^3 , C_+^4 , F_1 , and Ω . Although the manifold is two dimensional, it is necessary to visualise it in both (B, A, X) - and (B, A, Y) -projections because it exists in a four-dimensional space. Shown on $W_{\Sigma_0}^s$ is an orbit segment \mathbf{u} (magenta curve) representative of those used to compute $W_{\Sigma_0}^s$. The orbit segment \mathbf{u} starts at a given B and ends at Ω with maximum integration time. It has a fast approach to S^3 in X and Y before approaching mainly in the A -direction and then, finally, remaining close to C^3 for $O(1)$ slow time; this is evidence of a timescale splitting between A , and X and Y .

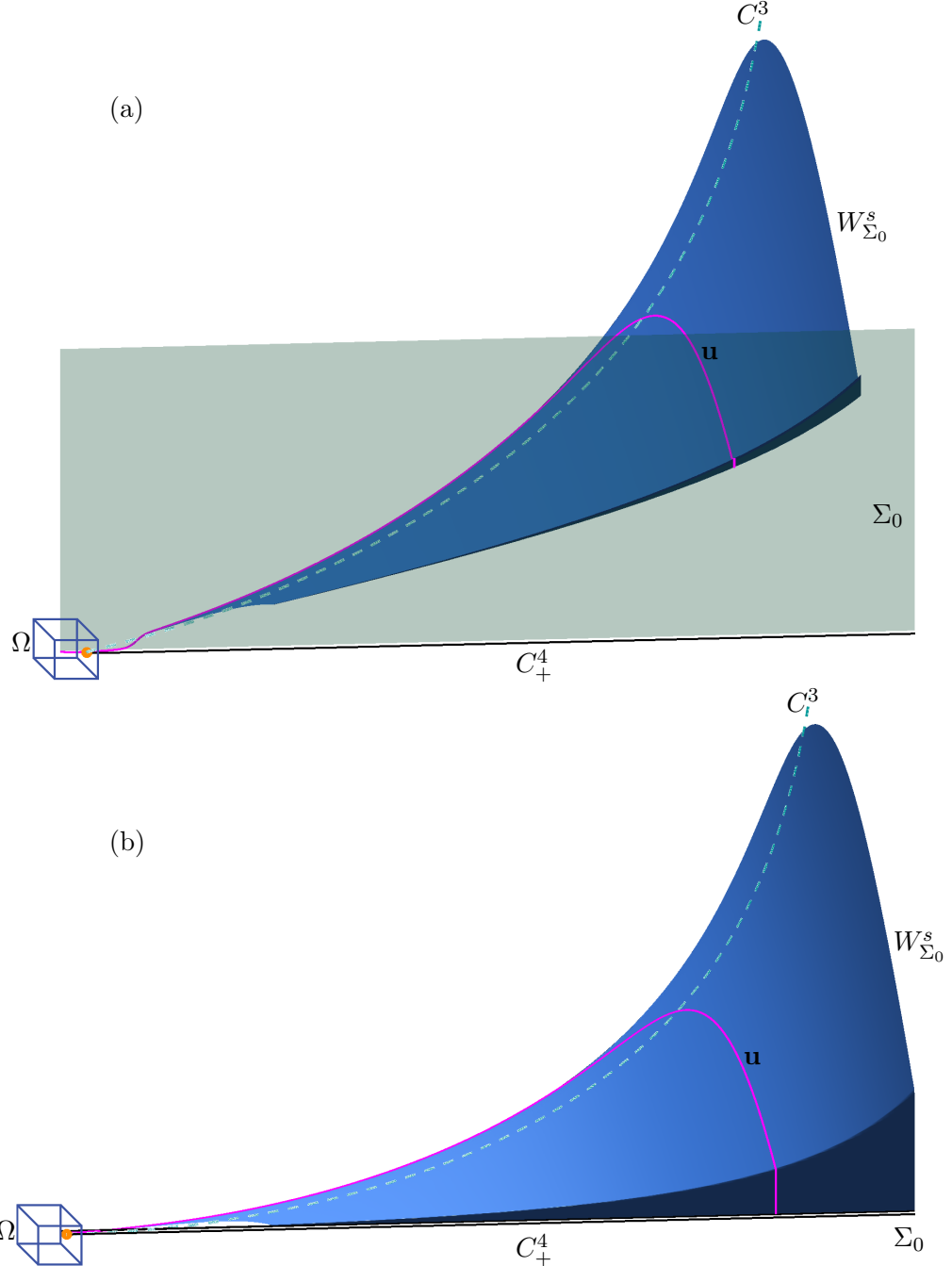


Fig. 4. The submanifold $W_{\Sigma_0}^s$ (light blue surface) of $W^s(S^3)$, shown in projection onto (B, A, X) -space (a) and onto (B, A, Y) -space (b); also shown are a representative orbit segment \mathbf{u} (magenta curve), the plane Σ_0 (mint surface and line), Ω (represented by a blue cube), C^3 , C_+^4 , and F_1 .

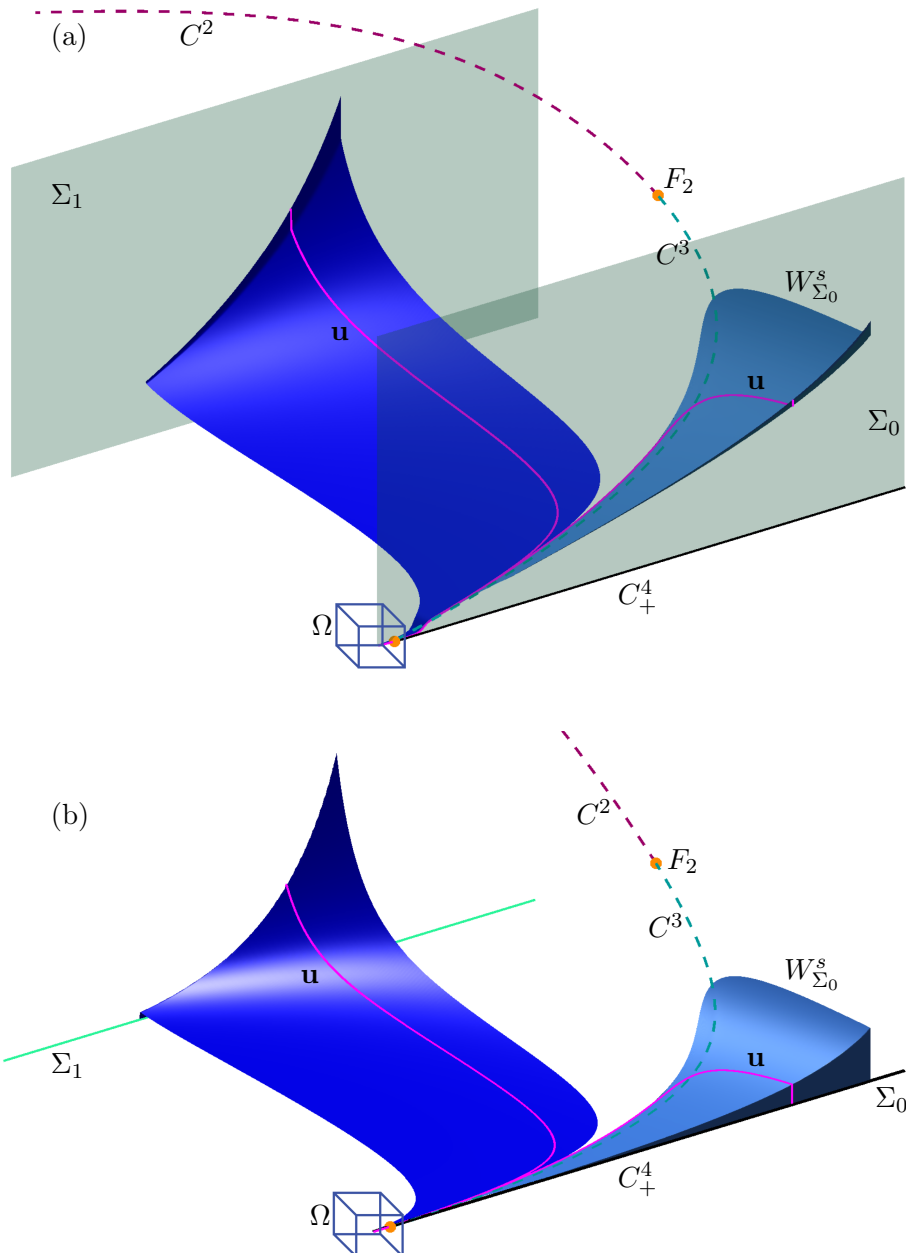


Fig. 5. The submanifolds $W_{\Sigma_0}^s$ (blue surface) and $W_{\Sigma_1}^s$ (light blue surface) of W^s , shown in projection onto (B, A, X) -space (a) and onto (B, A, Y) -space (b); also shown are representative orbit segments \mathbf{u} (magenta curves), the planes Σ_0 (mint surface and line) and Σ_1 (mint surface and line), and Ω (represented by a blue cube), C^2 , C^3 , C_+^4 , F_1 , and F_2 .

Figure 5 shows $W_{\Sigma_0}^s$ (light blue surface) together with one other submanifold $W_{\Sigma_1}^s$ (blue surface) of W^s in projection onto (B, A, X) -space and (B, A, Y) -space; here Σ_1 (mint surface) is given by $A = 2.0$ and $Y = 0.0$. The surface Σ_1 appears as a line in panel (b) because it is defined by constant A and X . The submanifold $W_{\Sigma_1}^s$ is an example of a submanifold on the other side of C with respect to the variable A ; compare with Figure 3(d). A representative magenta orbit segment on $W_{\Sigma_1}^s$ is shown approaching S^3 mainly from the X - and Y -directions, before approaching mostly in the A -direction.

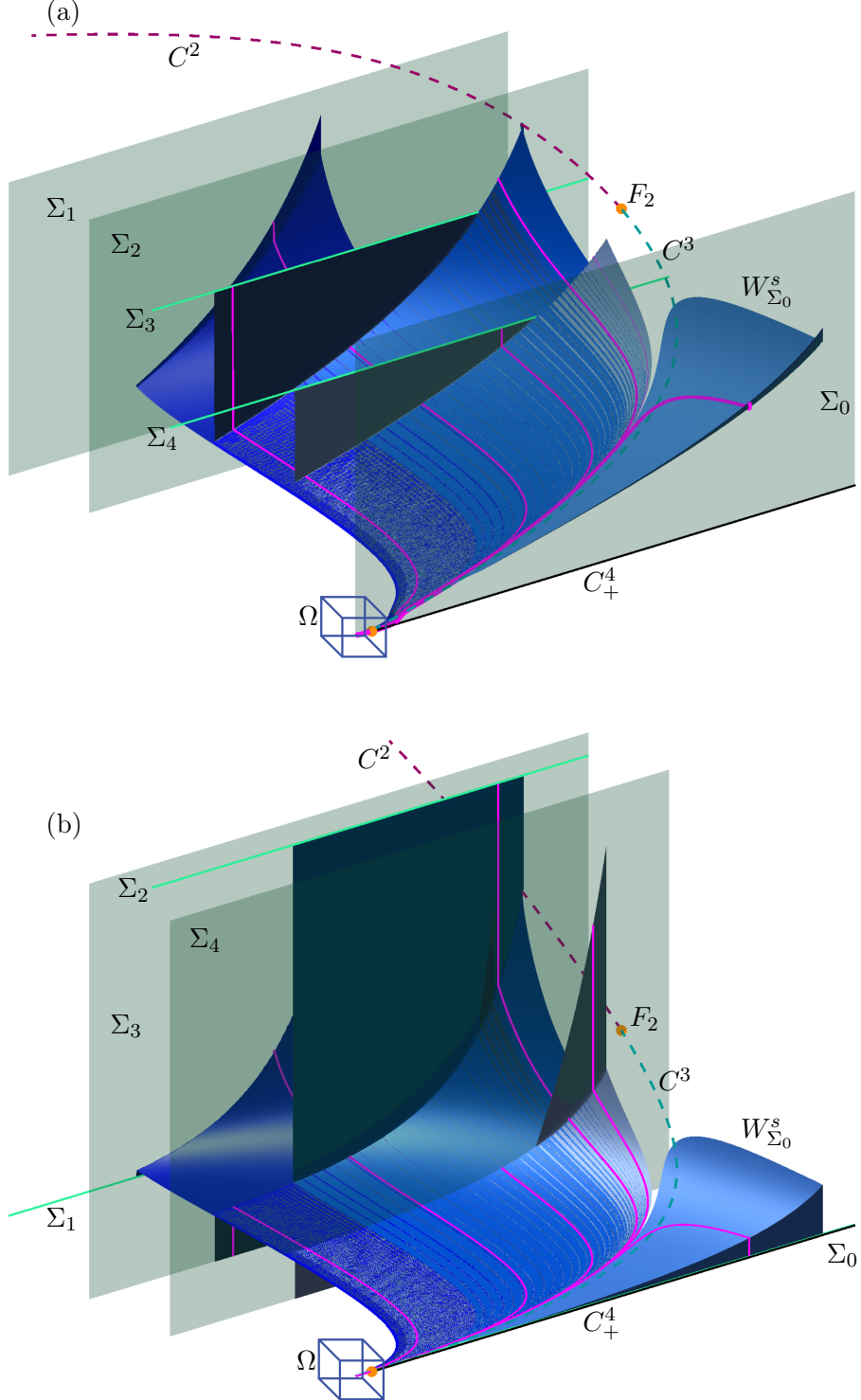


Fig. 6. The submanifolds from Figure 5 with three additional submanifolds $W_{\Sigma_i}^s$ (blue surfaces) of W^s for $2 \geq i \leq 4$ in projection onto (B, A, X) -space (a) and (B, A, Y) -space (b); also shown are representative orbit segments \mathbf{u} (magenta curves), the planes Σ_i (mint surfaces and lines), and Ω (represented by a blue cube), C^2 , C^3 , C_+^4 , F_1 , and F_2 .

Figure 6 shows the two submanifolds of W^s from Figure 5 with three additional submanifolds $W_{\Sigma_i}^s$ (blue surfaces) and the planes Σ_i (mint surfaces) that define them. Also shown are C^3 , C_+^4 , F_1 , and Ω . The additional submanifolds were selected with Σ_2 given by $A = 4.0$ and $Y = 0.75$, Σ_3 given by $A = 4.0$ and $X = 0.75$, and Σ_4 given by $A = 6.0$ and $X = 0.5$. Note that Σ_2 appears as a line in panel (b) because it is

defined by constant values of A and Y . Similarly, Σ_3 and Σ_4 appear as lines in panel (a) because they are defined by constant A and X . Orbit segments in Figure 6 again approach S^3 in the X - and Y -directions before approaching in the A -direction. This is responsible for regions where different submanifolds are extremely close to each other. In fact, these surfaces are so close that Matlab cannot distinguish them properly. Different choices of B_{in} and B_{out} also cause some submanifolds to extend farther than others in the B -direction.

Overall this section and its figures demonstrate that we can reliably compute any number of submanifolds W_Σ^s with conditions (5), (6), and (7) and the homotopy steps outlined above. Together, these two-dimensional submanifolds provide an understanding of the dynamics inside $W^s(S^3)$.

3.3. Definition and computation of $W^u(S^2)$

We can define S^2 and $W^u(S^2)$ similarly to how we defined S^3 and $W^s(S^3)$. The values for B_{in} and B_{out} are chosen such that $[B_{\text{out}}, B_{\text{in}}] \subset (B_q, B_H)$ where $B_q = 0.323$ and $B_H = 0.897$ are the B -values of the saddle equilibrium q and the Hopf point H shown, respectively, as a green cross and a pink dot in Figures 1, 3, and 7. Note that in these figures, the flow near S^2 is toward q ; hence, to the right of $W^u(q)$ the flow is to the left. Our choice of $B_{\text{out}} > B_q$ is to avoid a change in direction of the flow associated with q .

To compute a submanifold of $W^u(S^2)$ we use slightly different boundary conditions and homotopy steps compared to those used for $W^s(S^3)$ in light of two complicating challenges arising from q and H . Orbit segments near S^2 may increase in integration time by approaching $W^s(q)$ or by following the attracting slow manifold associated with C_-^4 backwards in time. We define a submanifold of $W^u(S^2)$ with boundary conditions that ensure that computed orbit segments do not demonstrate these behaviours and only increase in integration time by approaching S^2 .

To define S^2 and $W^s(S^2)$, we define a three-dimensional cylinder \mathcal{D}^u that is transverse to the flow and to $E^s(C^2)$. To this end, we choose a radius r and for each $B_p \in [B_{\text{in}}, B_{\text{out}}]$ define the two-dimensional sphere in the subspace $\{\omega \in \mathbb{R}^4 \mid B = B_p\}$ centred at p and with radius r ; here $p \in C^2$ is the unique point such that $p_B = B_p$. More formally,

$$D_r^u(B_p) = \{w \in \mathbb{R}^4 \mid w_B = B_p, \|w - p\| = r\}.$$

Then

$$\mathcal{D}^u = \bigcup_{B_p \in [B_{\text{out}}, B_{\text{in}}]} D_r^u(B_p),$$

is a three-dimensional cylinder. A smooth, one-parameter family of orbit segments of (1) is then given by the property that each orbit segment remains inside \mathcal{D}^u for an $O(1)$ amount of slow time, exits \mathcal{D}^u via $D_r^u(B_p)$ for some $B_p \in [B_{\text{out}}, B_{\text{in}}]$ and ends in some plane Σ . We denote by W_Σ^u those parts of the orbit segments that exit \mathcal{D}^u in the fast direction. The earlier parts that evolve mostly in the B -direction inside \mathcal{D}^u for $O(1)$ slow time are approximate segments of S^2 . If such an earlier part of the orbit segment includes a fast entrance into \mathcal{D}^u , that fast part lies on $W^s(S^2)$ in good approximation.

We compute the submanifold W_Σ^u again as a one-parameter family of orbit segments \mathbf{w} satisfying the rescaled equation (4). Orbit segments $\mathbf{w} \in W_\Sigma^u$ must satisfy the boundary conditions

$$\mathbf{w}(1) \in \Sigma, \tag{10}$$

$$\mathbf{w}(0) \in \Phi = E^u(p_0) \times [0, 1, 0, 0]^{\text{tr}}, \tag{11}$$

$$\mathbf{w}(0)_B = \hat{B}, \tag{12}$$

where $p_0 \in C^2$ is such that $p_{0B} \in (B_{\text{out}}, B_{\text{in}})$ and $\hat{B} > B_{\text{in}}$. Equations (10) and (11) are analogous to equations (5) and (6) from section 3.2. Equation (12) serves the purpose of preventing \mathbf{w} from increasing

in integration time by following the attracting slow manifold associated with C_-^4 backwards in time; it has no analogue in section 3.2. Equations (10), (11), and (12) define four conditions on solutions of (4) so that there is a one-parameter family of solutions to this 2PBVP. We denote the two-dimensional submanifold given by this one-parameter family by W_Σ^u .

Note that the above conditions preclude the selection of \mathbf{w} with maximal integration time as was done in section 3.2 with equation (7). In the case that we would like to impose a condition of maximum integration time, we may substitute for (10), the two conditions

$$\mathbf{w}(1) \in \mathcal{D}^u, \quad (13)$$

and

$$T = T^B, \quad (14)$$

where for each $B_p \in [B_{\text{out}}, B_{\text{in}}]$, the time T^B is the maximum integration time of an orbit segment that permanently exits \mathcal{D}^u at $B = B_p$ while satisfying (11) and (12). Equation (13) imposes one condition on $\mathbf{w}(1)$, one less condition than equation (10), allowing us to also impose equation (14). Equations (11), (12), (13), and (14) define four conditions on solutions of (4) so that there is again a one-parameter family of solutions to this 2PBVP. We denote the two-dimensional submanifold given by this one-parameter family by W_r^u .

Once an initial \mathbf{w} satisfying one of the 2PBVPs is found, it is possible to sweep out a submanifold W_Σ^u or W_r^u by continuing \mathbf{w} with varying $\mathbf{w}(1)_B$ and T_B . The challenge is, once again, the computation via homotopy steps of an initial orbit segment satisfying the boundary conditions.

In the first homotopy step, we choose the point $p_0 = (p_{0A}, p_{0B}, p_{0X}, p_{0Y}) \in C^2$ by fixing $p_{0B} = B_0 \in [B_{\text{out}}, B_{\text{in}}]$. We impose condition (11) as well as the condition

$$\mathbf{w}(1) \in \chi = \{\omega \in \mathbb{R}^4 \mid \omega_A = p_{0A}, \omega_B = p_{0B}, \omega_Y = p_{0Y}\}. \quad (15)$$

The point p_0 is then a solution to (11) and (15) for $T = 0$. We increase \mathbf{w}_B with T as a free parameter and stop the continuation when $\mathbf{w}_B = \widehat{B}$. The value of \mathbf{w}_B is fixed from this step onwards. We define the two-dimensional space

$$\Phi_{\widehat{B}} = \Phi \cap \{\omega \in \mathbb{R} \mid \omega_B = \widehat{B}\}.$$

In the second homotopy step, we substitute equation (15) for (10) with $\Sigma = \{\omega \in \mathbb{R}^4 \mid \omega_A = p_{0A}, \omega_Y = p_{0Y}\}$ and impose (12). The orbit segment \mathbf{w} at the end of the first homotopy step is then a solution to this 2PBVP defined by (4), (10), (11), and (12). It is in the second homotopy step that we decide whether to compute a submanifold W_Σ^u or W_r^u . If our aim is to compute W_Σ^u , all that remains to compute an initial \mathbf{w} lying on the manifold is to move Σ to a desired location as in section 3.2.

To compute W_r^u we increase T until $\mathbf{w}(1) \in \Sigma \cap \mathcal{D}^u$. This is detected as $\mathbf{w}(1)$ reaching a distance of r away from the point $p \in C^2$ such that $p_B = \mathbf{w}_B$. We denote the endpoint coordinates $\mathbf{w}(1)_B$ and $\mathbf{w}(1)_X$ by \widetilde{B} and \widetilde{X} , respectively, at the end of this step.

In the event that $D_r(\widetilde{B})$ contains a locus of points at which the flow is tangent to it, we perform a third homotopy step to increase \widetilde{B} until the flow is transverse to $D_r(\widetilde{B})$. This is achieved by imposing conditions (11), (12), and (13) on \mathbf{w} at the end of the second homotopy step and then increasing \mathbf{w}_B while keeping T as a free parameter.

In the final homotopy step, we replace condition (13) with

$$\mathbf{w}(1) \in \Theta = D_r^u(\widetilde{B}) \cap \{\omega \in \mathbb{R} \mid \omega_X = \widetilde{X}\}. \quad (16)$$

The orbit segment \mathbf{w} at the end of the second homotopy step (or the third homotopy step if one was necessary) is then a solution to the 2PBVP defined by (4), (11), (12), and (16). We then increase T until $T = T^B$, which is detected as a fold in integration time. The resulting orbit segment \mathbf{w} lies on W_r^u .

Once an initial orbit segment \mathbf{w} on either W_Σ^u or W_r^u is found, we may sweep out the remaining part of the submanifold by increasing and decreasing \mathbf{w}_B and keeping T as a free parameter.

Figure 7 illustrates in projection onto (B, A) -space, the adjusted homotopy steps for computing W_r^u . Each panel shows an enlargement of C from Figure 1 near C^2 with additional information for the computation. We choose $p_0 = (0.940272, 0.7, 1.492271, 1.342954)$ which lies on C^2 . In the first homotopy step, we impose condition (15), which imposes three conditions on $\mathbf{w}(1)$, as well as condition (11), which imposes one restriction on $\mathbf{w}(0)$. Panel (a) shows a sketch of an intermediate \mathbf{w} (forest green curve) in the first homotopy step; here the one-dimensional line χ is sketched in mint and the three-dimensional Φ is sketched as a mint prism. The B -coordinate of $\mathbf{w}(0)$ is increased with T as a free parameter. The continuation is stopped when $\mathbf{w}(0)_B = \hat{B}$ for $\hat{B} = 1.0$. In the second homotopy step, we impose (10), (11), and (12), increasing $\mathbf{w}(1)_B$ with T as a free parameter until $\mathbf{w}(1)$ intersects \mathcal{D}^u for $r = 0.7$. We are not required to perform an additional homotopy step because $D_r(\hat{B})$, in this case, does not contain a locus points at which the flow is tangent to it. Figure 7(b) shows a sketch of the numerical set up before the final homotopy step; here the one-dimensional closed curve Θ is sketched in mint and $\Phi_{\hat{B}}$ is sketched as a mint cross. We then impose (11), (12), (13) and (14) and increase T . The continuation is stopped when $T = T^B$ which is detected as a fold. The resulting orbit segment lies on W_r^u . We can then sweep out the rest of the submanifold W_r^u by continuing the fold in integration time for increasing and decreasing $\mathbf{w}(1)_B$.

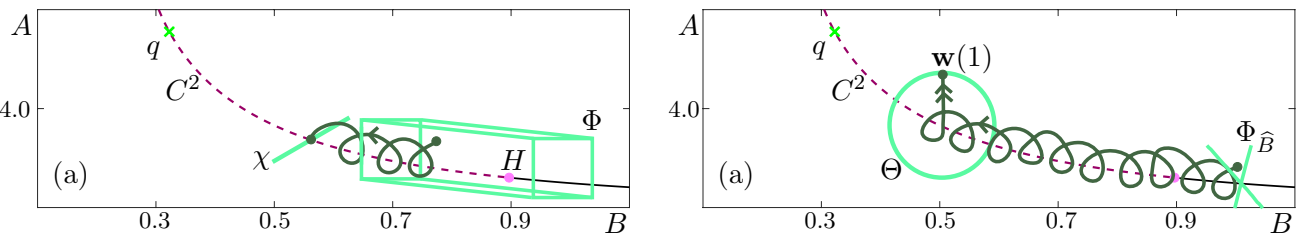


Fig. 7. A sketch in projection onto the (B, A) -plane of the homotopy steps for the computation of submanifolds W_r^u of $W^u(S^2)$. Also shown are C^2 , C_-^4 , H , q , and the orbit segment \mathbf{w} is shown as a forest green curve in each panel. Panel (a) is a sketch of an intermediate \mathbf{w} in the first homotopy step with χ (mint line) and Φ (mint prism); panel (b) is a sketch of the start of the final homotopy step with Θ (mint circle) and $\Phi_{\hat{B}}$ (mint cross).

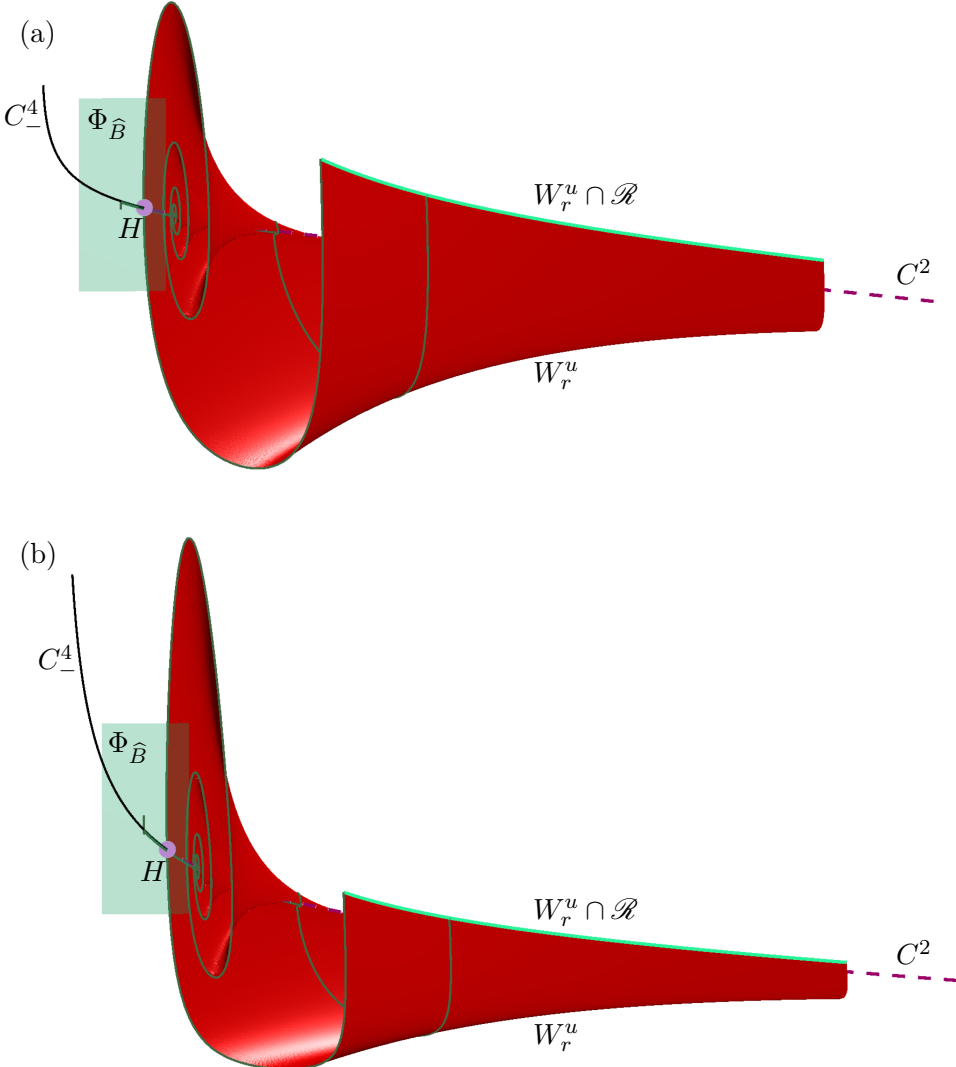


Fig. 8. The submanifold W_r^u (red surface) of $W^u(S^2)$ for $r = 0.7$ shown in projection onto (B, A, X) -space (a) and (B, A, Y) -space (b); note that the view is rotated compared to previous figures. Also shown are two representative orbit segments w (forest green curves) on W_r^u , the two-dimensional space $\Phi_{\hat{B}}$ (mint surface), the one-dimensional intersection $W_r^u \cap \mathcal{D}^u$ (mint curve), and C^2 , C_-^4 , and H .

Figure 8 shows two projections of the submanifold W_r^u for $r = 0.7$ with $W_r^u \cap \mathcal{D}^u$ (mint curve) and $\Phi_{\hat{B}}$ (mint surface). Note that $W_r^u \cap \mathcal{D}^u$ is simply the curve traced out by $w(1)$. To facilitate viewing, the view is rotated compared to previous figures. Two example orbit segments w are plotted and a subset of C^2 (dashed raspberry curve) is shown. From this angle, the radius of \mathcal{D}^u may, to some readers, appear to decrease with decreasing $w(1)_B$. This is due to the eye's erroneous association of points $w(1)$ with points $p \in C^2$ such that $p_B < w(1)_B$. Due to the spiralling nature of W_r^u , we only show one such submanifold for ease of visualization.

4. A heteroclinic connection between two saddle slow manifolds

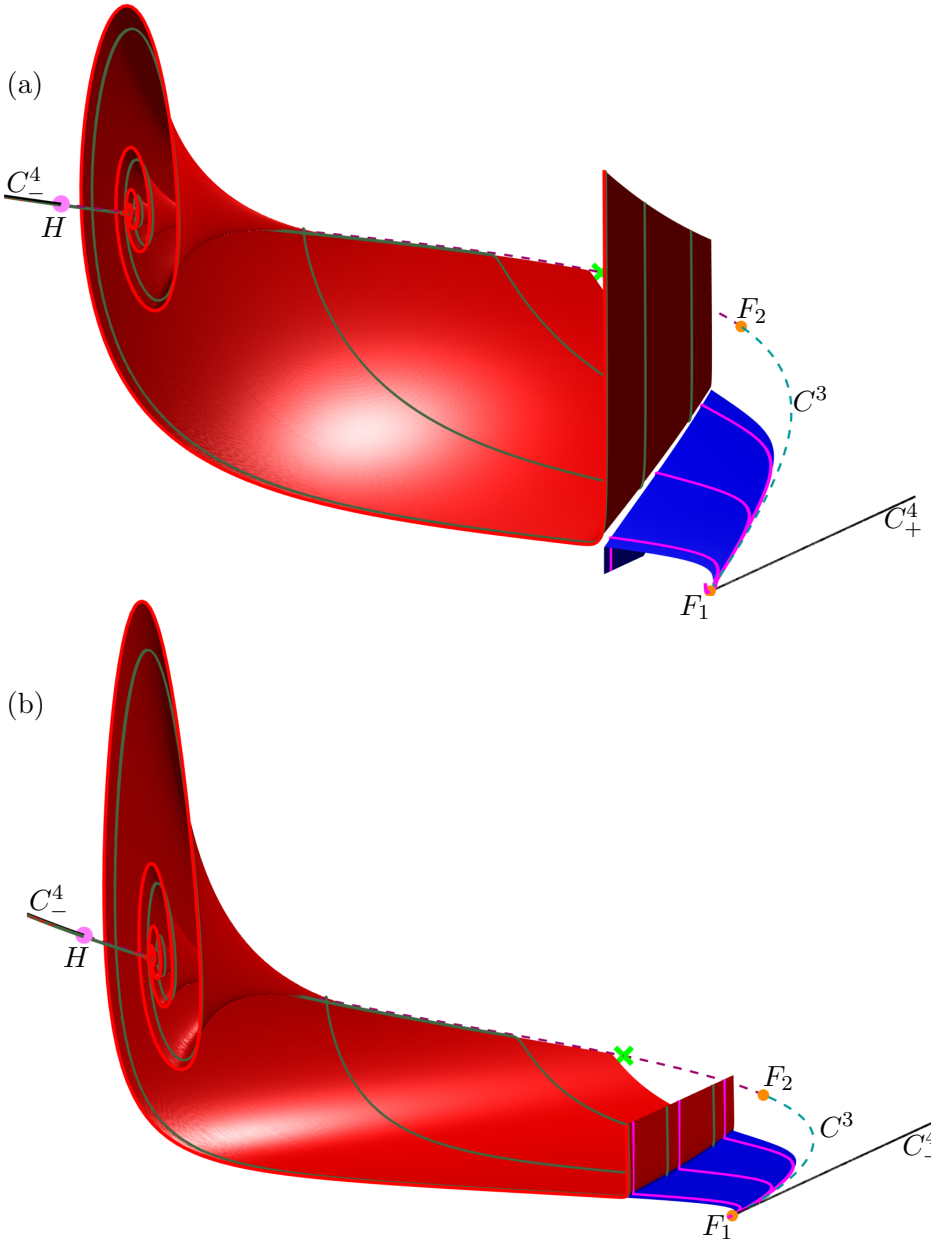


Fig. 9. The submanifold $W_{\Sigma_5}^u$ (red surface) of $W^u(S^2)$ and the submanifold $W_{\Sigma_5}^s$ (blue surface) of $W^s(S^3)$ in projection onto (B, A, X) -space (a) and onto (B, A, Y) -space (b). Representative orbit segments $\mathbf{w} \in W_{\Sigma_5}^u$ and $\mathbf{u} \in W_{\Sigma_5}^s$ are plotted in forest green and magenta, respectively; also shown are C^2 , C^3 , C_{\pm}^4 , F_1 , F_2 , H , and q (which is partially obscured by the two-dimensional submanifold $W_{\Sigma_5}^u$).

The stable manifold of S^3 computed for the reduced system in [Desroches *et al.*, 2009] stretches backward in time to reach S^2 , suggesting the existence of a surface of heteroclinic connections from S^2 to S^3 . In the full system (1), such a surface would be a two-dimensional submanifold of both $W^s(S^3)$ and $W^u(S^2)$ which we denote \mathcal{H} . Supporting the argument for the existence of \mathcal{H} is the fact that two three-dimensional objects in a four-dimensional space may intersect generically in a two-dimensional manifold. It follows, then, that the three-dimensional $W^s(S^3)$ and the three-dimensional $W^u(S^2)$ likely intersect in a two-dimensional surface of heteroclinic connections \mathcal{H} . The issue is to see whether this is actually the

case by finding the surface of connections \mathcal{H} . A natural way forward is to consider \mathcal{H} as a one-parameter family of concatenations of orbit segments $\mathbf{w} \in W^u(S^2)$ with $\mathbf{u} \in W^u(S^3)$.

A first idea is to compute two two-dimensional submanifolds W_Σ^u and W_Σ^s up to a suitable choice of a single two-dimensional section Σ . However, these two two-dimensional objects do not generically intersect in a four-dimensional space. Figure 9 demonstrates this difficulty. The chosen section $\Sigma_5 = \{\omega \in \mathbb{R}^4 \mid \omega_A = 6.0, \omega_Y = 0.5\}$ yields the submanifolds $W_{\Sigma_5}^s$ (blue surface) and $W_{\Sigma_5}^u$ (red surface) shown in Figure 9. Representative orbit segments \mathbf{w} (forest green curves) and \mathbf{u} (magenta curves) are shown coming toward each other mostly in the A -direction before diverging away from each other in the faster X - and Y -directions. Although the submanifolds appear to intersect in the (B, A, Y) -projection in Figure 9(b), we can see from the (B, A, X) -projection in Figure 9(a) that the $W_{\Sigma_5}^s$ and $W_{\Sigma_5}^u$ in fact miss each other in the four-dimensional phase space. Nevertheless, we are encouraged by the closeness of $W_{\Sigma_5}^u$ and $W_{\Sigma_5}^s$ that suggests that a surface \mathcal{H} of connecting orbits should exist nearby.

We turn to Lin's method to find the actual surface of connecting orbits \mathcal{H} . Lin's method has been used in parameter continuation to locate connections between equilibria and/or periodic orbits [Lin, 1989; Krauskopf & Rieß, 2008; Zhang *et al.*, 2012]. We use it here in a novel way to locate structurally stable connections between S^2 and S^3 for the system parameters given in Table 1.

We begin by choosing a three-dimensional section \mathcal{L} , called a Lin section, that divides the four-dimensional phase space into two regions such that C^3 lies in one region and C^2 lies in the other. More specifically, the Lin section \mathcal{L} is defined by a constant value of A that is chosen so that \mathcal{L} intersects C to the left of $W^u(q)$ in the (B, A) -projection; this choice of \mathcal{L} allows us to compute the largest possible portion of \mathcal{H} to the right of $W^u(q)$. Inside \mathcal{L} we choose a unit vector \mathbf{v}_Z with the generic property that it is not tangent to either $W^u(S^2)$ or $W^s(S^3)$. The vector \mathbf{v}_Z is called a Lin vector and the space Z spanned by \mathbf{v}_Z the associated Lin space. We then use the methods outlined in section 3 to compute $\mathbf{u} \in W^s(S^3)$ and $\mathbf{w} \in W^u(S^2)$ such that

$$\mathbf{u}(0) \in \mathcal{L} \quad (17)$$

and

$$\mathbf{w}(1) \in \mathcal{L}. \quad (18)$$

Additionally, we require that

$$\mathbf{u}(0) - \mathbf{w}(1) \in Z.$$

Importantly, the signed distance between $\mathbf{u}(0)$ and $\mathbf{w}(1)$ inside Z , given by

$$\eta = [\mathbf{u}(0) - \mathbf{w}(1)] \cdot \mathbf{v}_Z, \quad (19)$$

is a regular test function. Note that $|\eta| = \|\mathbf{u}(0) - \mathbf{w}(1)\|$. A pair of orbit segments (\mathbf{w}, \mathbf{u}) with

$$\eta = 0 \quad (20)$$

is then a connection between S^2 and S^3 . Hence, finding a zero of η is the way of finding a connecting orbit in \mathcal{H} .

To implement $\mathbf{u}(0), \mathbf{w}(1) \in Z$, we define unit normal vectors $\mathbf{n}_1 \perp \mathbf{v}_Z$ and $\mathbf{n}_2 \perp \mathbf{v}_Z$ such that $\mathbf{n}_1 \perp \mathbf{n}_2$ and impose conditions

$$[\mathbf{u}(0) - \mathbf{w}(1)] \cdot \mathbf{n}_1 = 0 \quad (21)$$

and

$$[\mathbf{u}(0) - \mathbf{w}(1)] \cdot \mathbf{n}_2 = 0. \quad (22)$$

Equations (21) and (22) ensure that $\mathbf{w}(1) - \mathbf{u}(0)$ remains in Z . Conditions (19) and (20) together ensure that $\mathbf{w}(1) = \mathbf{u}(0)$. Once an initial (\mathbf{w}, \mathbf{u}) satisfying the above conditions is found, the surface \mathcal{H} can be swept out, for example by varying $\mathbf{w}(1)_B$ with $\mathbf{u}(0)_B$ and T as additional free parameters.

The challenge is, as always, the computation via homotopy steps of an initial pair (\mathbf{w}, \mathbf{u}) satisfying the required BCs. In the first homotopy step we compute $\mathbf{w} \in W_{\Sigma_{L_1}}^u$ and $\mathbf{u} \in W_{\Sigma_{L_2}}^s$ for $\Sigma_{L_1}, \Sigma_{L_2} \subset \mathcal{L}$,

requiring (5) and (8) for \mathbf{u} and (10), (11), and (12) for \mathbf{w} . In particular, (17) and (18) are then satisfied and we choose

$$\mathbf{v}_Z = \frac{\mathbf{u}(0) - \mathbf{w}(1)}{\|\mathbf{u}(0) - \mathbf{w}(1)\|},$$

which is a convenient choice of a vector that is (generically) transverse to $W^u(S^2)$ and $W^s(S^3)$. We then find the vectors \mathbf{n}_1 and \mathbf{n}_2 required for conditions (17) and (18). Once chosen, the vector \mathbf{v}_Z and normal vectors \mathbf{n}_1 and \mathbf{n}_2 remains fixed throughout the computations.

The conditions imposed in the first homotopy step define a two-parameter family of orbit segment pairs (\mathbf{w}, \mathbf{u}) that meet in \mathcal{L} along Z . In the second homotopy step, we now relax conditions (5) and (10), which respectively are two conditions each on \mathbf{u} and \mathbf{w} , and impose instead conditions (17) and (18), (19), (21) and (22). Conditions (17) and (18), respectively, impose one condition on \mathbf{u} and one condition on \mathbf{w} . Conditions (21) and (22) impose two condition on (\mathbf{w}, \mathbf{u}) . The number of boundary conditions imposed is hence the same as in the first homotopy step, and thus they define a two-parameter family of orbit segment pairs (\mathbf{w}, \mathbf{u}) . To choose a one-parameter family (\mathbf{w}, \mathbf{u}) from these, we impose the additional boundary condition

$$\mathbf{w}(1)_B = B_1, \quad (23)$$

where B_1 is the value of the B -coordinate of $\mathbf{w}(1)$ at the end of the first homotopy step. We now continue (\mathbf{w}, \mathbf{u}) as a solution to the 2PBVP defined by (8), (11), (17) and (18), (19) and (21), (22), and (23) with T and $\mathbf{u}(0)_B$ as free parameters. We monitor condition (19) and stop the continuation when $\eta = 0$, at which point condition (20) is satisfied and the concatenation of \mathbf{w} with \mathbf{u} is a connecting orbit segment in \mathcal{H} . We can then sweep out the portion of \mathcal{H} to the right of $W^u(q)$ in the (B, A) -projection by replacing condition (23) with (20), keeping $\mathbf{u}(0)_B$, $\mathbf{w}(1)_B$, and T as free parameters.

Figure 10 illustrates, step-by-step in projection onto the (B, A) -plane, the homotopy steps for computing the portion of \mathcal{H} to the right of $W^u(q)$. Each panel shows C from Figure 1 with $\mathcal{L} = \{\omega \in \mathbb{R}^4 \mid \omega_A = 6.0\}$ (charcoal line), $\mathbf{u} \in W_{\Sigma_{L_1}}^s$ (magenta curve), $\mathbf{w} \in W_{\Sigma_{L_2}}^u$ (forest green curve), the stable eigenspace $E^s(p_{out})$ (blue cross) from condition (8), the two-dimensional space $\Phi_{\hat{B}}$ (mint cross) from conditions (11) and (12), and additional information for the computation. In the first homotopy step, we choose $\Sigma_{L_1} = \{\omega \in \mathbb{R}^4 \mid \omega_A = 6.0, \omega_Y = -1.0\}$ and $\Sigma_{L_2} = \{\omega \in \mathbb{R}^4 \mid \omega_A = 6.0, \omega_Y = 3.0\}$. We compute \mathbf{w} so that $\mathbf{w}(1)_B = B_1 = 0.6$ in the second homotopy step. Figure 10(a) is a sketch of the numerical set-up at the end of the first homotopy step. The points $\mathbf{w}(1)$ and $\mathbf{u}(0)$ lie in the space Z (gold line) from conditions (21) and (22) at a distance η from each other. Panel (b) is a sketch of the numerical set up after the second homotopy step when $\mathbf{w}(1) = \mathbf{u}(0)$ and $\eta = 0$. The resulting pair (\mathbf{w}, \mathbf{u}) satisfy conditions (17) and (18)–(20) and their concatenation lies on the surface \mathcal{H} .

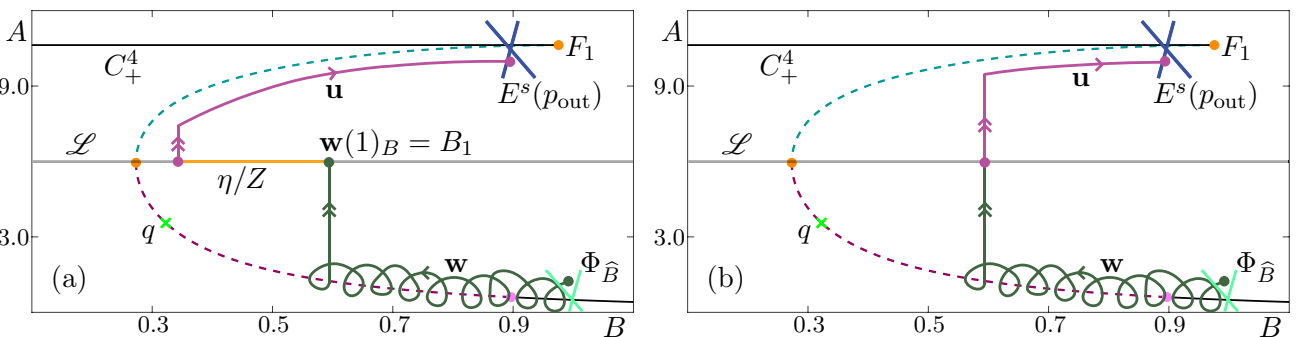


Fig. 10. A sketch in projection onto the (B, A) -plane of the numerical set up with Lin's method for the computation of \mathcal{H} to the right of $W^u(q)$. Also shown are C^2 , C^3 , C_\pm^4 , F_1 , F_2 , H , and q . Panel (a) shows a sketch at the end of the first homotopy step with $\mathbf{u} \in W_{\Sigma_{L_1}}^s$ (magenta curve), $\mathbf{w} \in W_{\Sigma_{L_2}}^u$ (forest green curve), $\Phi_{\hat{B}}$ from section 3.2, and the Lin space Z (gold line) in which the points $\mathbf{w}(1)$ and $\mathbf{u}(0)$ lie at a distance η from each other. Panel (b) shows \mathbf{w} and \mathbf{u} after the final homotopy step at which point $\eta = 0$ and $\mathbf{w}(1) = \mathbf{u}(0)$.

After these homotopy steps we use boundary conditions (17) and (18), (19), (20), and (21) and (22) to sweep out a one-parameter family of orbit segment pairs to obtain an accurate approximation of \mathcal{H} to the right of $W^u(q)$. Figure 11 shows the computed portion of \mathcal{H} (red/blue surface) with \mathcal{L} (charcoal plane) in projection onto (B, A, X) -space (a) and (B, A, Y) -space (b). Three concatenated orbit segment pairs (\mathbf{w}, \mathbf{u}) lying on \mathcal{H} are plotted in forest green for \mathbf{w} and magenta for \mathbf{u} . The portion of the surface swept out by \mathbf{w} is shown in red and that by \mathbf{u} in blue. Orbit segments lying on \mathcal{H} spiral slowly around S^2 before crossing the surface mostly in the direction parallel to the A -axis to reach and then slowly follow S^3 .

Figure 12 shows that the computed portion of \mathcal{H} is bounded by $W^u(q)$ (cardinal surface; this surface was computed with the BVP approach outlined in [Krauskopf *et al.*, 2007]). Here \mathcal{H} is coloured red near S^2 and blue near S^3 to illustrate that \mathcal{H} is both a submanifold of $W^u(S^2)$ and of $W^s(S^3)$; compare with Figure 11. Similarly, concatenated orbit segments (\mathbf{w}, \mathbf{u}) are plotted fading from forest green to magenta. Orbits on \mathcal{H} clearly follow S^2 on the slow timescale, before traversing across \mathcal{H} on an intermediate timescale and then following S^3 on the slow timescale. As this figure shows, the saddle point q and its two-dimensional unstable manifold $W^u(q)$ bound the computed portion of \mathcal{H} . Notice how the connecting orbits nearest $W^u(q)$ follow this two-dimensional surface to come very close to q , before slowly following S^2 . Hence, we computed the part of \mathcal{H} to this side of q as closely to $W^u(q)$ as possible.

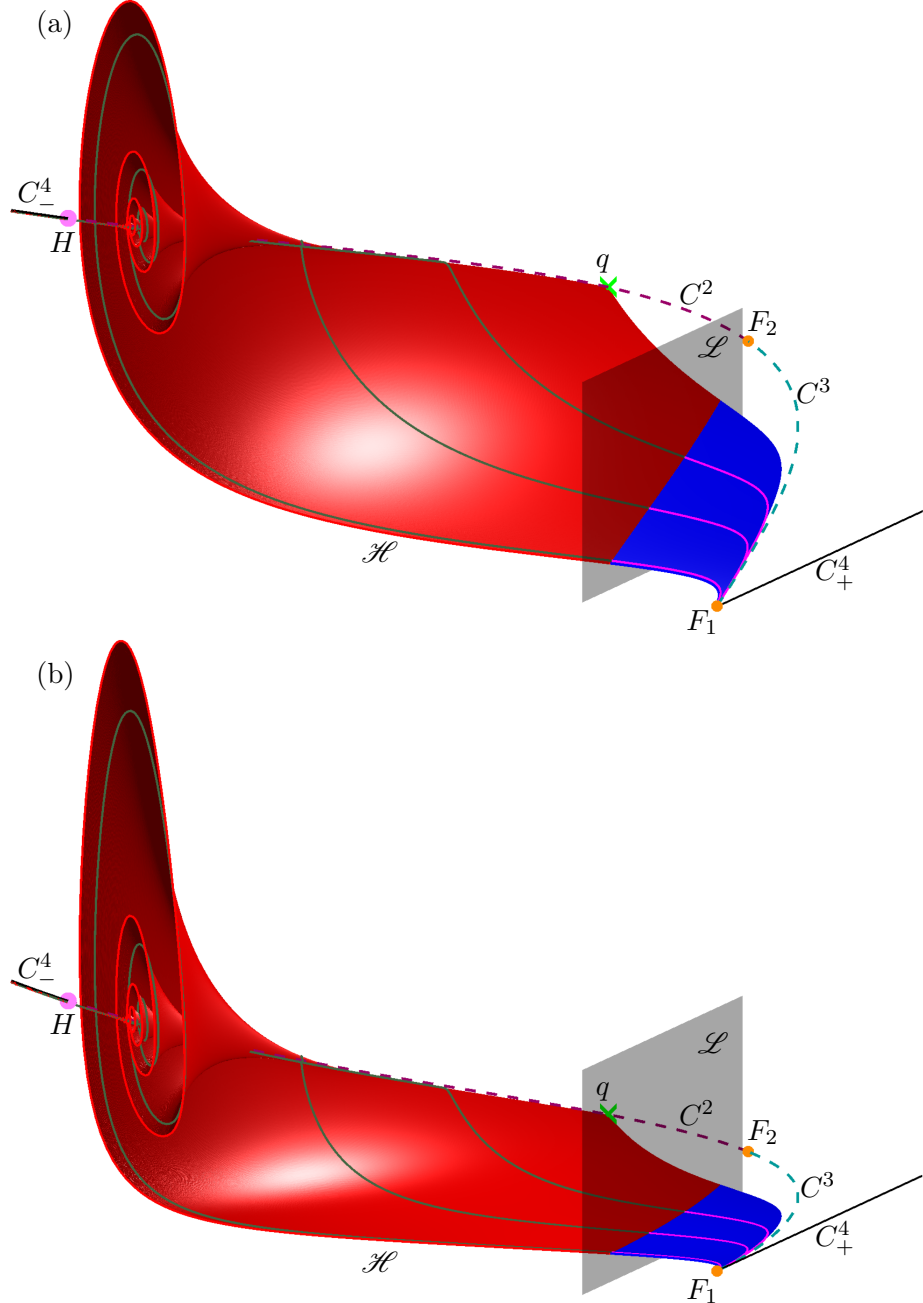


Fig. 11. The surface of heteroclinic connections \mathcal{H} (red/blue surface) and the Lin section \mathcal{L} (charcoal surface) in projection onto (B, A, X) -space (a) and onto (B, A, Y) -space (b). The portion of $W^u(S^2)$ swept out by the \mathbf{w} is shown in red and the portion of $W^s(S^3)$ swept out by the \mathbf{u} is shown in blue. Also shown are representative orbit segments pairs (\mathbf{w}, \mathbf{u}) (forest green/magenta curves), C^2 , C^3 , C_\pm^4 , F_1 , F_2 , H and q which is partially obscured by \mathcal{H} and \mathcal{L} .

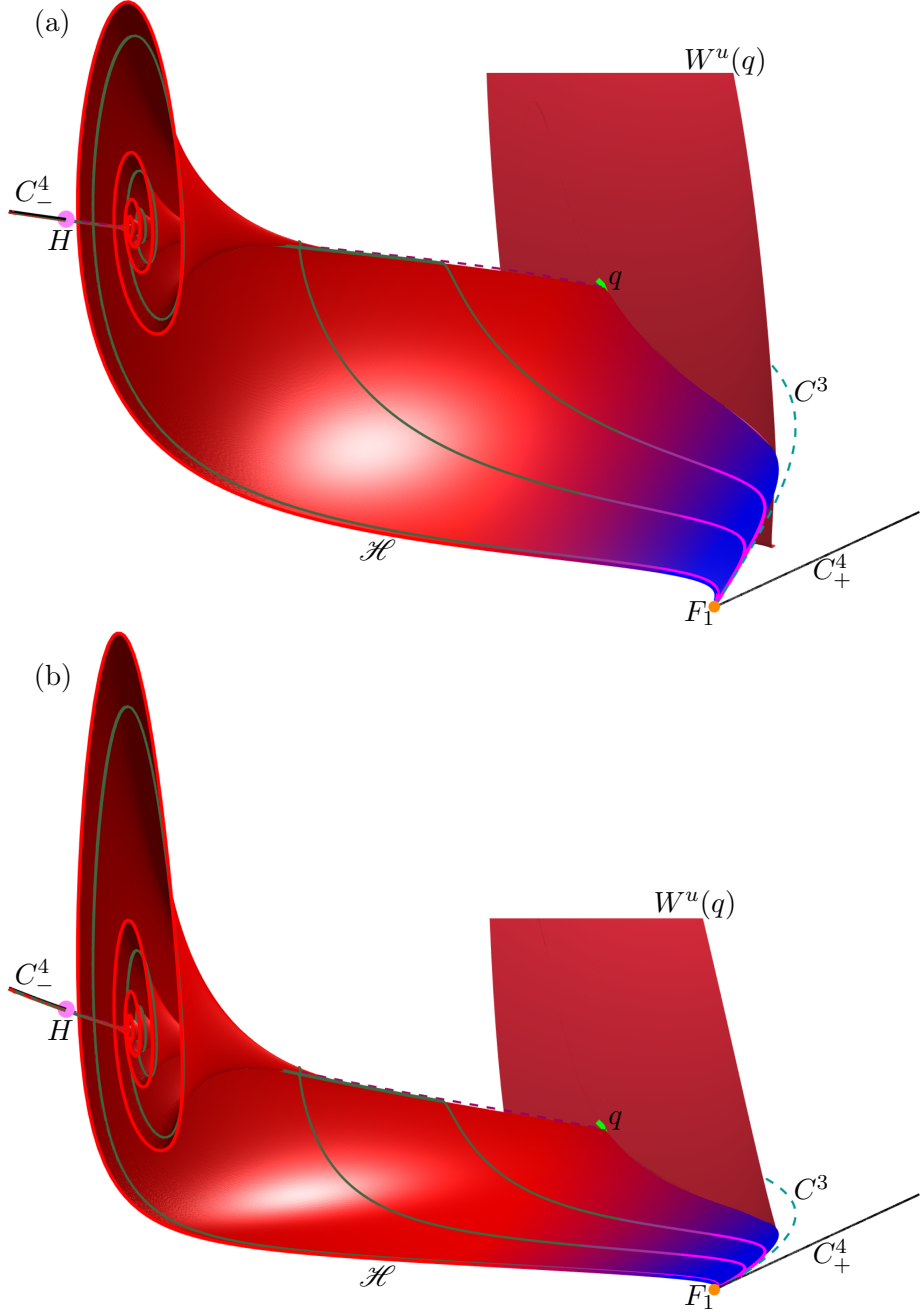


Fig. 12. The computed portion of \mathcal{H} (red-blue fade surface) is shown in projection onto (B, A, X) -space (a) and onto (B, A, Y) -space (b) with $W^u(q)$ (cardinal surface). The unstable manifold $W^u(q)$ bounds the computed portion of \mathcal{H} . Also shown are representative orbit segment pairs (\mathbf{w}, \mathbf{u}) (forest green-magenta fade curves), C^2 , C^3 , C_{\pm}^4 , F_1 , F_2 , H and q which is partially obscured by \mathcal{H} and $W^u(q)$. Here $\varepsilon = 0.0037$ as in Table 1.

5. Computing the surface of heteroclinic connections in the singular limit

We now consider the limiting surface \mathcal{H}_0 of connecting orbits from C^2 to C^3 for $\varepsilon = 0$. Since then system (1) reduces to the three-dimensional system (2) in which B is a parameter, the surface \mathcal{H}_0 is the one-parameter family, parametrized by B , of connections between the saddle equilibria of (2) on C^2 and on C^3 , respectively. It is simple to sweep out \mathcal{H}_0 with varying B once an initial connection is found for fixed B . This is exactly the situation addressed in [Krauskopf *et al.*, 2007] and we now briefly explain how this approach can be used for our purposes.

We compute \mathcal{H}_0 as the one parameter family of concatenated orbit segment pairs, denoted (\mathbf{w}, \mathbf{u}) , of the rescaled system

$$\frac{d\mathbf{u}}{ds} = TG(\mathbf{u}), \quad (24)$$

where now $\mathbf{u}(s) = (A(s), X(s), Y(s)) \in \mathbb{R}^3$ is the vector of chemical concentrations, G is the right-hand side of (2), and T is the integration time on the fast timescale.

We again turn to Lin's method to find an initial orbit segment pair lying on \mathcal{H}_0 via homotopy steps. We begin by choosing a $\hat{B} \in (B_{\text{in}}, B_{\text{out}})$ corresponding to points $\hat{p}^2 \in C^2$ and $\hat{p}^3 \in C^3$. A two-dimensional Lin section, denoted $\widehat{\mathcal{L}}$, is chosen such that, for any value of $\hat{B} \in (B_{\text{in}}, B_{\text{out}})$ it divides the three-dimensional phase space into a region containing \hat{p}^2 and a region containing \hat{p}^3 . Inside $\widehat{\mathcal{L}}$, we choose a Lin vector \mathbf{v}_Z with the property that it is not tangent to $W^u(\hat{p}^2)$ or $W^s(\hat{p}^3)$. The Lin vector \mathbf{v}_Z then defines the associated Lin space Z . We then use the methods outlined in [Krauskopf *et al.*, 2007] to compute $\mathbf{w} \in W^u(\hat{p}^2)$ and $\mathbf{u} \in W^s(\hat{p}^3)$ satisfying appropriate boundary conditions. We first impose two conditions,

$$\mathbf{u}(1) \in \Upsilon^3 = \{\omega \in \mathbb{R}^3 \mid \|\hat{p}^3 - \omega\| = r_3\} \cap E^s(\hat{p}^3), \quad (25)$$

and

$$\mathbf{w}(0) \in \Upsilon^2 = \{\omega \in \mathbb{R}^3 \mid \|\hat{p}^2 - \omega\| = r_2\} \cap E^u(\hat{p}^2), \quad (26)$$

where radii r_2 and r_3 are chosen such that the closed curves Υ_2 and Υ_3 are close to \hat{p}^2 and \hat{p}^3 , respectively. We next impose the conditions

$$\mathbf{u}(0) \in \widehat{\mathcal{L}}, \quad (27)$$

and

$$\mathbf{w}(1) \in \widehat{\mathcal{L}}. \quad (28)$$

while additionally requiring that

$$\mathbf{w}(1) - \mathbf{u}(0) \in Z.$$

The signed distance between $\mathbf{w}(0)$ and $\mathbf{u}(1)$ inside Z is given by

$$\eta = [\mathbf{w}(0) - \mathbf{u}(1)] \cdot \mathbf{v}_Z \quad (29)$$

which is a regular test function. As before, a pair of orbit segments (\mathbf{w}, \mathbf{u}) with

$$\eta = 0 \quad (30)$$

is then a connection between \hat{p}^2 and \hat{p}^3 . To implement $\mathbf{u}(0), \mathbf{w}(1) \in Z$, we now define a single unit normal vector $\mathbf{n} \perp \mathbf{v}_Z$ and impose the condition

$$[\mathbf{u}(0) - \mathbf{w}(1)] \cdot \mathbf{n} = 0 \quad (31)$$

which ensures that $\mathbf{w}(1) - \mathbf{u}(0)$ remains in Z . Conditions (29) and (30) together ensure that $\mathbf{u}(0) = \mathbf{w}(1)$, while (25) and (26) ensure that $\mathbf{w} \in W^u(\hat{p}^2)$ and $\mathbf{u} \in W^s(\hat{p}^3)$.

Again, two homotopy steps are used to find an initial pair (\mathbf{w}, \mathbf{u}) of connecting orbits. First, we use the method outlined in [Krauskopf *et al.*, 2007] to compute $\mathbf{w} \in W^u(\hat{p}^2)$ and $\mathbf{u} \in W^s(\hat{p}^3)$ such that (27) and (28) are satisfied; then \mathbf{w} and \mathbf{u} automatically satisfy conditions (25) and (26). We then choose \mathbf{v}_Z again as

$$\mathbf{v}_Z = \frac{\mathbf{u}(0) - \mathbf{w}(1)}{\|\mathbf{u}(0) - \mathbf{w}(1)\|}$$

and find the unit normal \mathbf{n} required for condition (31); which then remain fixed for throughout the computation.

By construction, the pair (\mathbf{w}, \mathbf{u}) at the end of the first homotopy step is a solution to the 2PBVP defined by (25), (26), (27), (28), (29), and (31); keeping η , T , $\mathbf{u}(0)_B$, and $\mathbf{w}(1)_B$ as free parameters allows us to close the Lin gap and satisfy $\eta = 0$, at which point the concatenation of \mathbf{w} with \mathbf{u} forms an orbit segment in \mathcal{H}_0 .

Specifically we choose $\hat{B} = 0.4$, $r_3 = 0.0001$, and $\widehat{\mathcal{L}} = \{\omega \in \mathbb{R}^4 \mid \omega_A = 6.0\}$. We then sweep out \mathcal{H}_0 by imposing condition (30) and increasing and decreasing the parameter \hat{B} , keeping T , $\mathbf{w}(1)_B$, $\mathbf{u}(0)_B$, and the coordinates of \hat{p}^2 and \hat{p}^3 as free parameters. Note that we are not limited by the location of $W^u(q)$ in the computation of \mathcal{H}_0 . However, we are faced with an additional challenge due to a change in the type of equilibria on C^2 because q is just one of the equilibria on C^2 . For $\hat{B} < 0.476858$, the saddle \hat{p}^2 has real eigenvalues, for $\hat{B} > 0.476858$ the eigenvalues are complex conjugate, causing spiralling of \mathbf{w} to increase as \hat{B} approaches H_B . A larger mesh size is needed to numerically approximate \mathbf{w} with more spirals. On the other hand, keeping the mesh size constant throughout the computation is an advantage when one wants to render the overall surface \mathcal{H}_0 . We keep the mesh fixed, but allow the radius r_2 to increase as follows

$$r_2 = \begin{cases} 0.0001 & \hat{B} < 0.476858 \\ 0.521789(\hat{B} - 0.476858) + 0.0001 & \hat{B} > 0.476858 \end{cases}$$

Hence, r_2 increases linearly from 0.0001 to 0.2 between $\hat{B} = 0.476858$ and $\hat{B} = 0.86$, that is, where p^2 is complex conjugate. By making r_2 larger in this way in regions where orbit segments exhibit more spiralling near C^2 , we avoid computing tightly spiralling pieces of the orbit segments and thus eliminate the need for a larger mesh size.

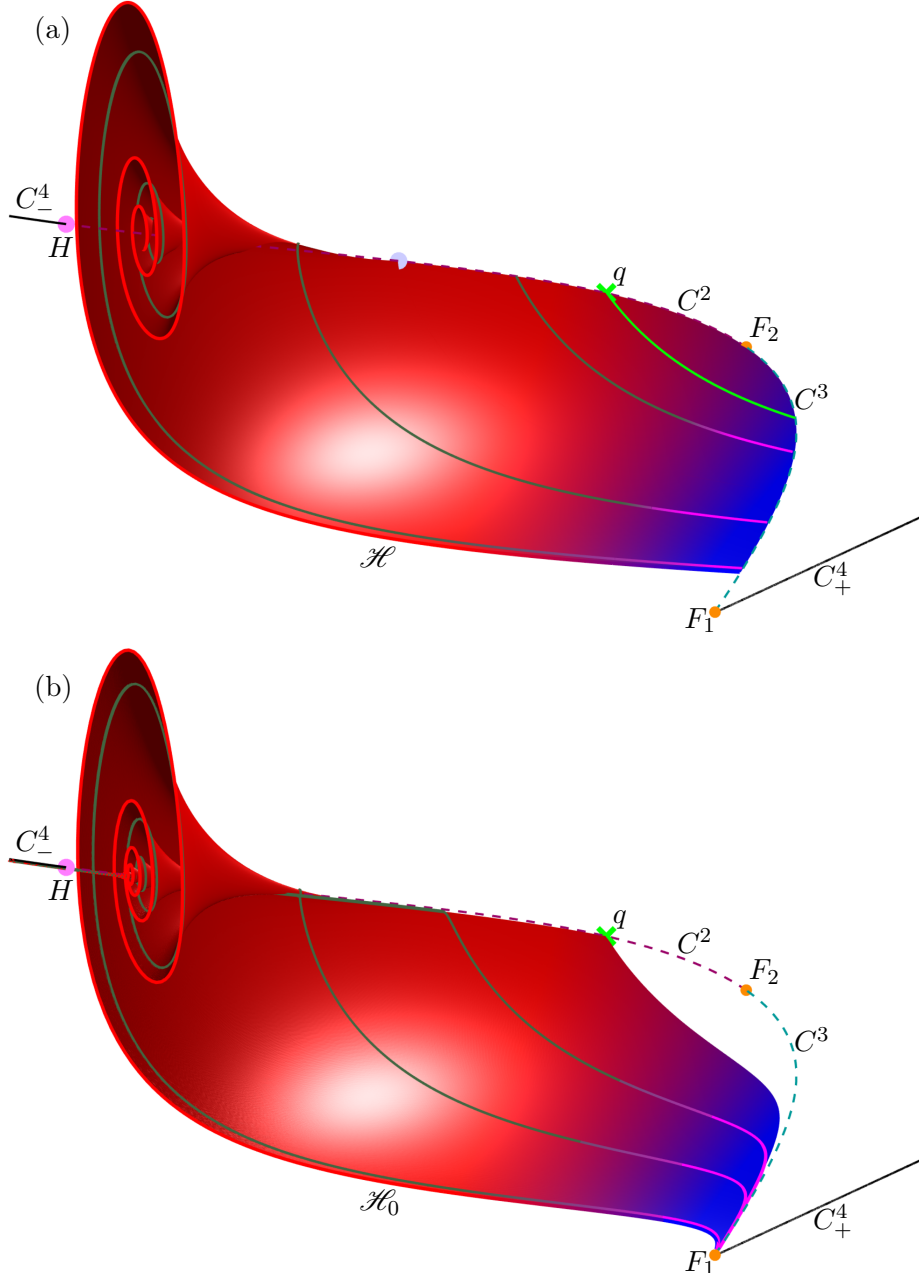


Fig. 13. Projections onto (B, A, X) -space of the portion of \mathcal{H}_0 lying in the region $B < 0.781$ (red-blue fade surface) (a) and \mathcal{H} for $\varepsilon = 0.0037$ (red-blue fade surface) (b). Also shown in panel (a) for $\varepsilon = 0$ are the intersection $W^u(q) \cap \mathcal{H}_0$ (green curve) for $\varepsilon = 0$ and the point $p \in C^2$ (periwinkle dot) with $p_B = 0.476858$ where the eigenvalues become complex conjugate. Both panels also show representative orbit segments (forest green-magenta fade curves), q , C^2 , C^3 , C_\pm^4 , F_1 , F_2 , and H .

Figure 13 shows the two computed surfaces \mathcal{H}_0 for $\varepsilon = 0$ (red-blue fade surface) in panel (a) in comparison with the surface \mathcal{H} for $\varepsilon = 0.0037$ (red-blue fade surface) in panel (b) in projection into (B, A, X) -space. To aid a visual comparison with \mathcal{H} in panel (b), we show only the portion of \mathcal{H}_0 in panel (a) that lies in the region $B < 0.781$. Notice how \mathcal{H}_0 starts to spiral increasingly from the equilibrium (periwinkle dot) on C^2 where the eigenvalues become complex conjugate. In both panels, three representative orbit segments are shown on the surface (forest green-magenta fade curves). Unlike orbit segments on \mathcal{H} , for $\varepsilon = 0$ orbit segments on \mathcal{H}_0 do not exhibit any drift in the direction along C^2 and C^3 , respectively. The intersection of \mathcal{H}_0 with the singular $W^u(q)$ (green curve) is analogous to the border of \mathcal{H} near q ; compare with Figure 12. Notice due to the B -dependence of r_2 , the surface does not spiral all the way into C^3 in panel (a).

5.1. Distance of \mathcal{H} from \mathcal{H}_0

Fenichel theory states that \mathcal{H} will converge to \mathcal{H}_0 with decreasing ε [Fenichel, 1979]. A natural question is then how close \mathcal{H}_0 and \mathcal{H} are to each other for $\varepsilon = 0.0037$. To investigate the distance between \mathcal{H}_0 and \mathcal{H} , we stratify the surfaces into intersections with sections $\Lambda = \{\omega \in \mathbb{R}^4 \mid \omega_B = \hat{B}\}$ for several values of \hat{B} . We denote intersections $\mathcal{H} \cap \Lambda$ and $\mathcal{H}_0 \cap \Lambda$ by $\mathcal{H}^{\hat{B}}$ and $\mathcal{H}_0^{\hat{B}}$, respectively. The integral norms between $\mathcal{H}^{\hat{B}}$ and $\mathcal{H}_0^{\hat{B}}$ are approximated to estimate the distance between \mathcal{H} and \mathcal{H}_0 .

Any $\mathcal{H}_0^{\hat{B}}$ can be readily obtained by including the requirement that $B = \hat{B}$ in the computation of \mathcal{H}_0 . Since we do not intend to render a surface after the computation of $\mathcal{H}_0^{\hat{B}}$, we can increase the mesh size in the computation and take $r_2 = 1 \times 10^{-3}$. The curve $\mathcal{H}_0^{\hat{B}}$ can be compared with the corresponding $\mathcal{H}^{\hat{B}}$ on \mathcal{H} . We can use a computer package such as MATLAB to approximate the intersection curve $\mathcal{H}^{\hat{B}} = \mathcal{H} \cap \Lambda$ with the data from the previously computed surface, however it's much more accurate and elegant to compute $\mathcal{H}^{\hat{B}}$ via continuation.

We follow the steps for computing \mathcal{H} and stop the continuation when $\mathbf{u}(0)_B = \hat{B}$ instead of sweeping out the entire surface. We swap conditions (17) and (18) for conditions

$$\mathbf{u}(0) \in \Lambda \tag{32}$$

and

$$\mathbf{w}(0) \in \Lambda \tag{33}$$

to sweep out the one-parameter family of pairs (\mathbf{w}, \mathbf{u}) satisfying (19), (20), (21), (22), (32), and (33) with varying $\mathbf{u}(0)_A$ and T . The curve $\mathcal{H}^{\hat{B}}$ is then taken to be the one-parameter family of $\mathbf{u}(0)$.

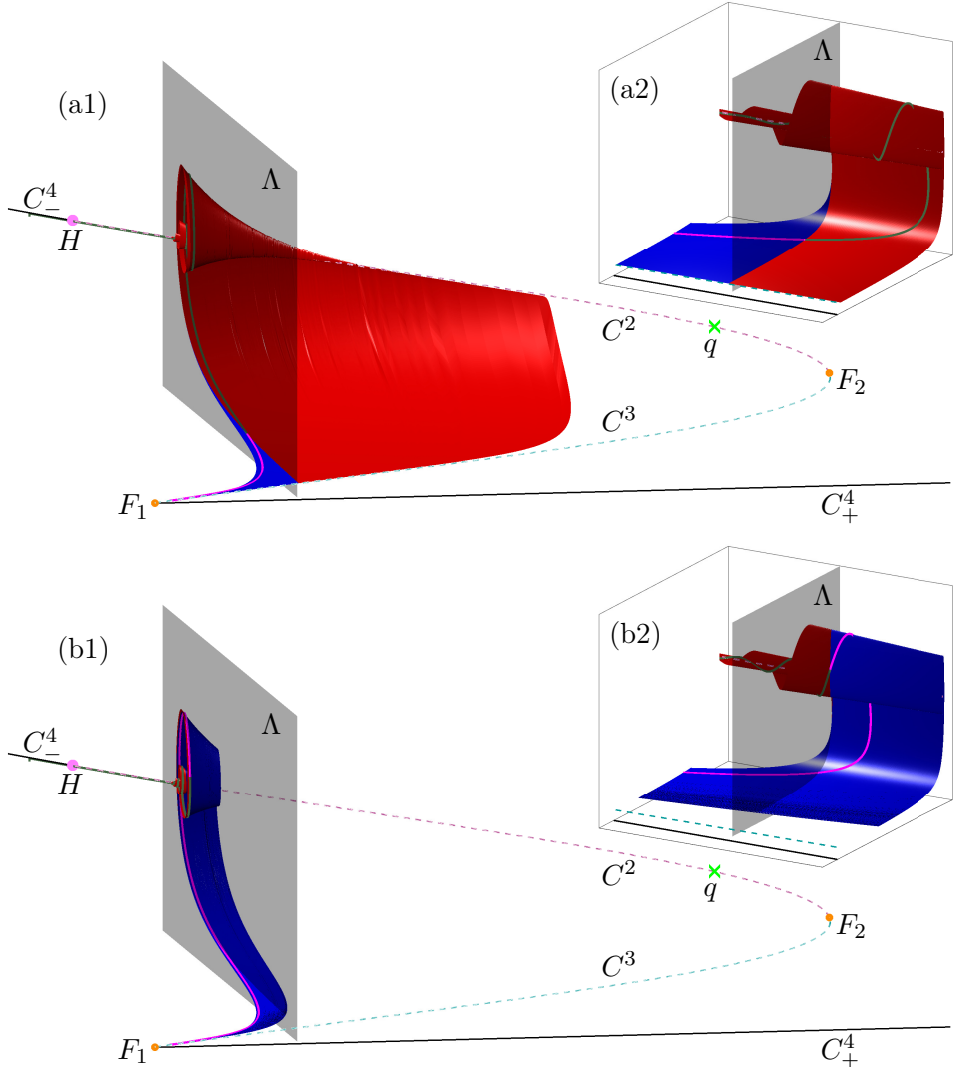


Fig. 14. Portions of the surface \mathcal{H} (red/blue surface) computed as a one-parameter family of (\mathbf{w}, \mathbf{u}) (forest green/magenta curves) with $\mathbf{u}(0)$ capturing the first intersection of (\mathbf{w}, \mathbf{u}) with Λ (charcoal surface) (a) and with $\mathbf{u}(0)$ capturing the second intersection of (\mathbf{w}, \mathbf{u}) with (b). Global views of the surface are shown in panels (a1) and (b1). Enlargements of the region near $\mathcal{H} \cap \Lambda$ are shown in panels (a2) and (b2). The full surface \mathcal{H} is not computed in either panel due to the backwards time contraction near C^2 rendering the $\mathbf{u}(0)$ near C^2 indistinguishable for different (\mathbf{w}, \mathbf{u}) pairs. Also shown are two representative (\mathbf{w}, \mathbf{u}) pairs (forest green/magenta curves), q , C^2 , C^3 , C_{\pm}^4 , F_1 , F_2 , and H .

When computing $\mathcal{H}^{\widehat{B}}$ with the above conditions, some orbit segments lying on \mathcal{H} are computed twice as distinct (\mathbf{w}, \mathbf{u}) pairs. This is due to a tangency with Λ of an orbit segment lying on \mathcal{H} that causes all except the tangent orbit segment to intersect Λ twice. Figure 14(a) shows \mathcal{H} computed with $\mathbf{u}(0)$ capturing the first intersection of orbit segments with Λ for $\widehat{B} = 0.75$. Figure 14(b) shows a portion of \mathcal{H} computed again with $\mathbf{u}(0)$ capturing the second intersection. Global views are shown in panels (a1) and (b1) and enlargements of the region near $\mathcal{H} \cap \Lambda$ are shown in panels (a2) and (b2). The entire surface is not computed in either panel because the backwards time contraction near C^2 causes many (\mathbf{w}, \mathbf{u}) pairs to have $\mathbf{u}(0)$ that are too similar to be distinguished by AUTO. Both panels show representative (\mathbf{w}, \mathbf{u}) (forest green/magenta curve), q , C^2 , C^3 , C_{\pm}^4 , F_1 , F_2 , and H .

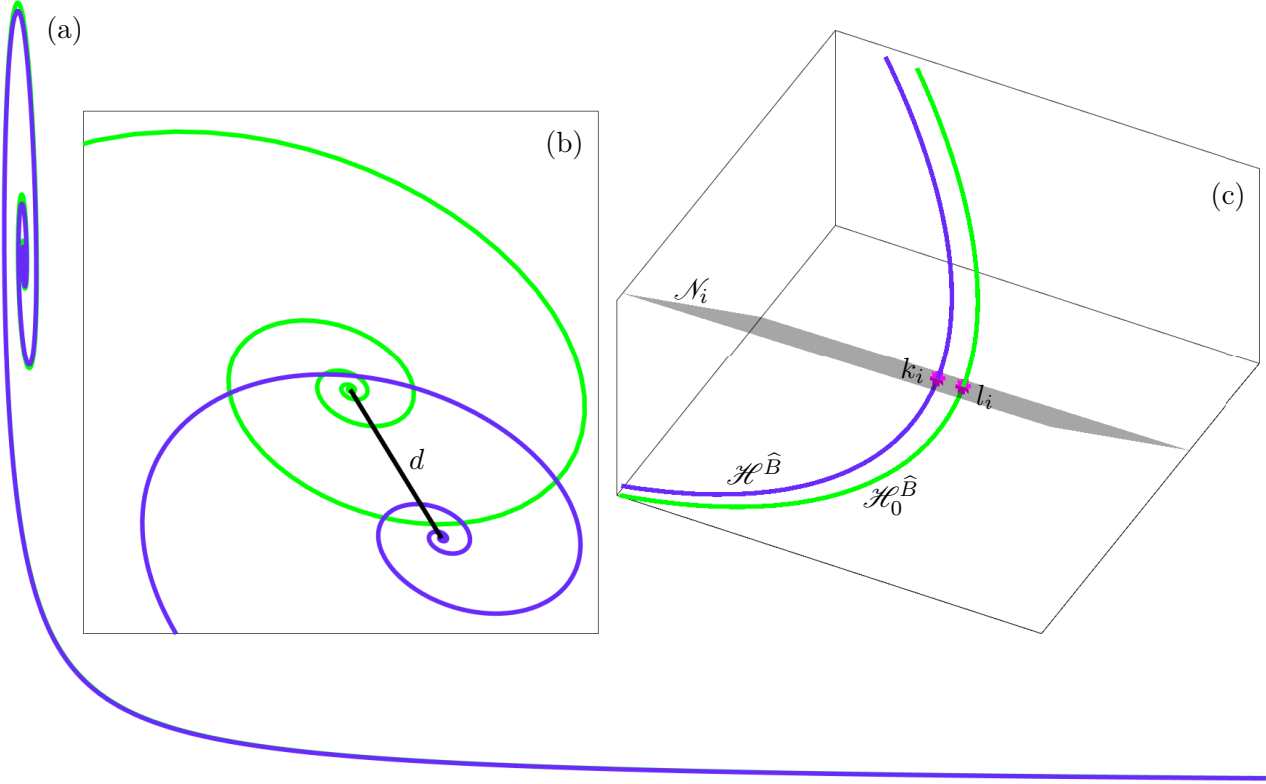


Fig. 15. Intersection curves $\mathcal{H}^{\widehat{B}}$ (royal purple) and $\mathcal{H}_0^{\widehat{B}}$ (lime green) for $\widehat{B} = 0.75$ projected onto the (A, X) -plane (a). An enlargement of the spiralling region near the endpoints of the curves is shown in panel (b) with the line of length d connecting them. Panel (c) shows a further enlargement of the spiralling region inside the (A, X, Y) -space, Λ , with the plane \mathcal{N}_i (charcoal surface) that is normal to $\mathcal{H}_0^{\widehat{B}}$ at the point l_i (magenta dot). The corresponding point k_i on $\mathcal{H}^{\widehat{B}}$ is also shown in magenta.

To approximate the integral norm between $\mathcal{H}^{\widehat{B}}$ and $\mathcal{H}_0^{\widehat{B}}$, we discretize the integral to a sum. For any point $l_i \in \mathcal{H}_0^{\widehat{B}}$, we want to find an associated point $k_i \in \mathcal{H}^{\widehat{B}}$. The integral norm between $\mathcal{H}^{\widehat{B}}$ and the truncated $\mathcal{H}_0^{\widehat{B}}$ is approximated with the formula

$$\sum_{i=1}^N \frac{1}{N} \|l_i - k_i\| \quad (34)$$

where N is the number of computed mesh points approximating $\mathcal{H}_0^{\widehat{B}}$. We must then choose an appropriate method for picking a k_i for each l_i . We pick a k_i to be an approximation of $\mathcal{H}^{\widehat{B}} \cap \mathcal{N}_i$ where \mathcal{N}_i is the plane normal to $\mathcal{H}_0^{\widehat{B}}$ at the point l_i . Figure 15 shows several zooms of $\mathcal{H}_0^{\widehat{B}}$ (lime green curve) and $\mathcal{H}^{\widehat{B}}$ (royal purple curve) for $\widehat{B} = 0.75$ projected onto the (A, X) -plane (a), (b) and in the full (A, X, Y) -space inside Λ (c). The global view of $\mathcal{H}^{\widehat{B}}$ and $\mathcal{H}_0^{\widehat{B}}$ is shown in panel (a). The curves appear closest in the flat region, except where $\mathcal{H}_0^{\widehat{B}}$ extends past $\mathcal{H}^{\widehat{B}}$ on the right-hand side of the projection. This is due to S^3 being $O(\varepsilon)$ away from C^3 . To accurately compare the curves, we truncate $\mathcal{H}_0^{\widehat{B}}$ at the first point l_i such that $\mathcal{N}_i \cap \mathcal{H}^{\widehat{B}}$ is non empty and call that point l_1 . The curves $\mathcal{H}^{\widehat{B}}$ and $\mathcal{H}_0^{\widehat{B}}$ differ the most in the region where they are spiralling. Panel (b) shows an enlargement near the endpoints of $\mathcal{H}_0^{\widehat{B}}$ and $\mathcal{H}^{\widehat{B}}$. The distance, d , between the endpoints on $\mathcal{H}_0^{\widehat{B}}$ and $\mathcal{H}^{\widehat{B}}$ is shown as a black line. It is again due to S^2 being $O(\varepsilon)$ away from C^2 . We truncate $\mathcal{H}_0^{\widehat{B}}$ at the l_i with a distance of $2d$ from the $\mathcal{H}_0^{\widehat{B}}$ endpoint and call that point l_N , as we take N to be the number of data points on the truncated curve. Panel (c) shows a further enlargement of the curves shown in panel (b) in the full (A, X, Y) -space, Λ . An example l_i (magenta dot)

is shown lying on the associated plane \mathcal{N}_i (charcoal surface) that intersects $\mathcal{H}^{\widehat{B}}$ at the point k_i (magenta dot).

We compute the k_i by first fitting splines Spl and Spl_0 to the mesh points approximating $\mathcal{H}^{\widehat{B}}$ and $\mathcal{H}_0^{\widehat{B}}$, respectively, shown in Figure 15. To fit Spl and Spl_0 , we use the built-in MATLAB function SPLINE. For each mesh point $l_i \in \mathcal{H}_0^{\widehat{B}}$ we then use the built-in MATLAB function FNDR with Spl_0 to compute the vector tangent to $\mathcal{H}_0^{\widehat{B}}$ at the point l_i . With the tangent vector, we define \mathcal{N}_i and compute the intersection of \mathcal{N}_i with Spl_0 as shown in Figure 15(c) where l_i and k_i are shown as magenta dots for a fixed value of i . For $i = 1$ in the flat region of $\mathcal{H}_0^{\widehat{B}}$, the intersection $Spl \cap \mathcal{N}_i$ is unique and our choice of k_i is obvious. In later regions where $\mathcal{H}^{\widehat{B}}$ and $\mathcal{H}_0^{\widehat{B}}$ are spiralling, intersections $Spl \cap \mathcal{N}_i$ are not always unique. We make a unique choice of k_i by requiring that it has the smallest arclength distance from k_{i-1} along $\mathcal{H}_0^{\widehat{B}}$. Some points k_i are outside the convolute of $\mathcal{H}_0^{\widehat{B}}$, however we still include them in our computation. In panel (c), the point k_i (magenta dot) lies on $\mathcal{H}^{\widehat{B}}$ where it is intersected by \mathcal{N}_i . The approximated integral norm between the two curves for $\widehat{B} = 0.75$ is 7.63856×10^{-3} .

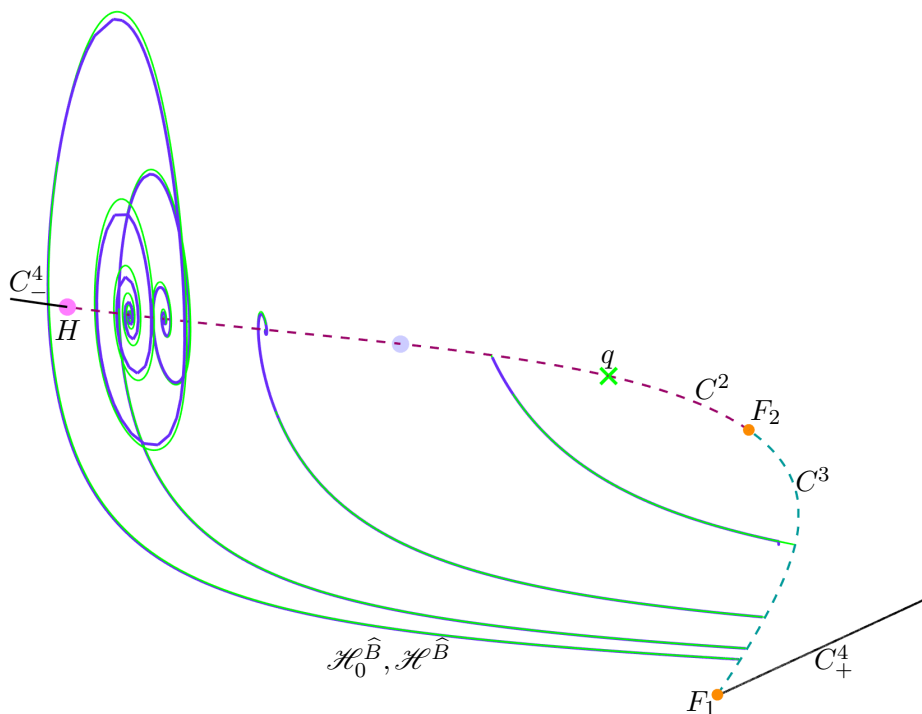


Fig. 16. Projection into the (A, X) -plane of the intersection curves $\mathcal{H}^{\widehat{B}}$ (royal purple) and $\mathcal{H}_0^{\widehat{B}}$ (lime green) of \mathcal{H} and \mathcal{H}_0 with section Λ for $\widehat{B} = 0.8$, $\widehat{B} = 0.75$, $\widehat{B} = 0.62$, and $\widehat{B} = 0.4$ (front to back). The curve $\mathcal{H}^{\widehat{B}}$ is visible behind $\mathcal{H}_0^{\widehat{B}}$ only in the region where the curves are spiralling.

Figure 16 shows curves $\mathcal{H}^{\widehat{B}}$ and $\mathcal{H}_0^{\widehat{B}}$ given by $\widehat{B} = 0.8$, $\widehat{B} = 0.75$, $\widehat{B} = 0.62$, and $\widehat{B} = 0.4$ (front to back) in projection into (B, A, X) -space. The difference in $\mathcal{H}^{\widehat{B}}$ and $\mathcal{H}_0^{\widehat{B}}$ is more pronounced for \widehat{B} closer to H_B because $\mathcal{H}^{\widehat{B}}$ and $\mathcal{H}_0^{\widehat{B}}$ spiral more as \widehat{B} approaches H_B . The integral norm is *findthislater* for $\widehat{B} = 0.8$, 1.153728×10^{-2} for $\widehat{B} = 0.62$, and 4.62565×10^{-4} for $\widehat{B} = 0.4$. Note that in this view $\mathcal{H}^{\widehat{B}}$ and $\mathcal{H}_0^{\widehat{B}}$ given by $\widehat{B} = 0.75$ are slightly obscured by the curves given by $\widehat{B} = 0.8$.

6. Implications for mixed-mode oscillation geometry

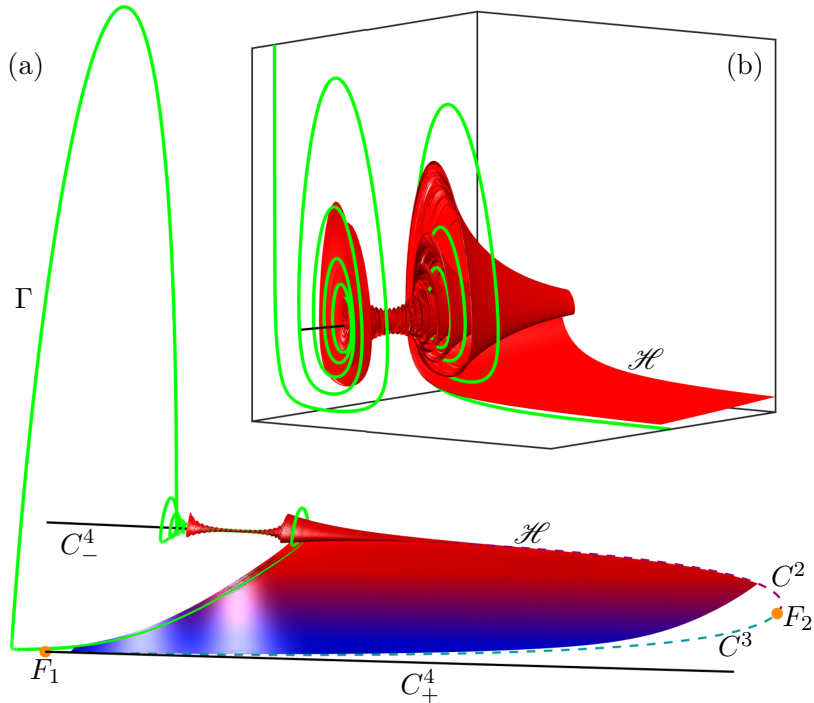


Fig. 17. The MMO Γ (green curve) and the surface of heteroclinic connections \mathcal{H} (red-blue fade) extended in backwards time past the Hopf bifurcation point H are shown in projection onto (B, A, X) -space. Panel (a) shows the global view of Γ tracking \mathcal{H} from C^2 to C^3 and making a LAO to C_-^4 . Panel (b) shows the subsequent slow passage of Γ through H . Also shown are q , C^2 , C^3 , C_\pm^4 , F_1 , F_2 , and H .

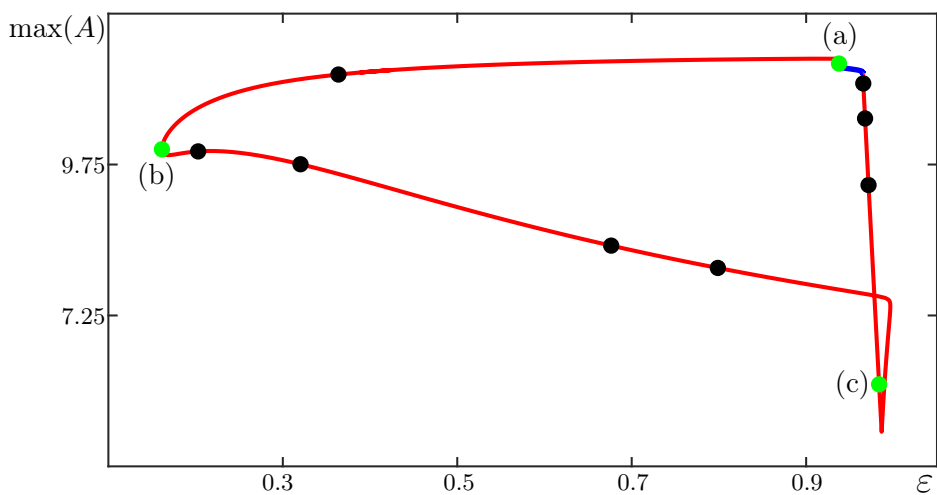


Fig. 18. The isola of MMO Γ over ε . The PO Γ is stable along the blue part and unstable along the red part of the isola. Green dots labeled (a), (b), and (c) correspond to Γ as shown in Figure 14.

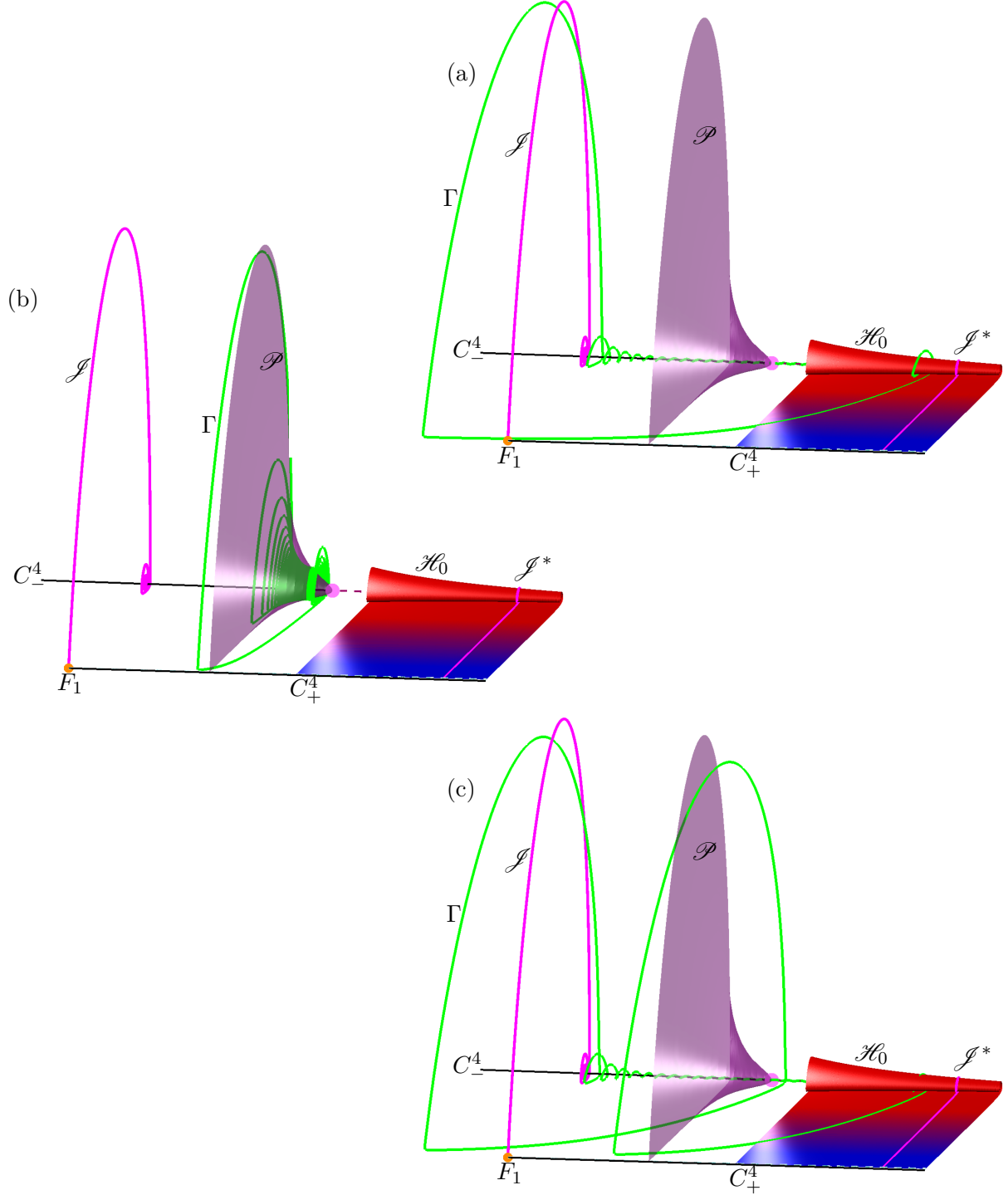


Fig. 19. Projections onto (B, A, X) -space of the portion of \mathcal{H}_0 (red-blue fade surface) lying in the region $B < 0.781$, of the jump back trajectory \mathcal{J} (magenta curve) and its dual \mathcal{J}^* (magenta curve), and of the surface of singular POs \mathcal{P} (midnight grape surface). Also shown are C^2 , C^3 , C_{\pm}^4 , F_1 , F_2 , and H . Panel (a) shows Γ (green curve) for the original value of ε . The entry and exit of Γ into the region of SAOs are near \mathcal{J} and \mathcal{J}^* , respectively. Panel (b) shows a representative Γ (green curve) that remains near \mathcal{P} in both the regions of SAOs and LAOs. Panel (c) shows a representative Γ (green curve) that has two LAOs. Entry and exits into the region of SAOs are again near \mathcal{J} and \mathcal{J}^* , respectively.

Figure 17 shows Γ (green curve) for the original value $\varepsilon = 0.0037$ in projection onto (B, A, X) -space with \mathcal{H} (red-blue fade surface) which is extended in backwards time past H . Also shown are q , C^2 , C^3 ,

C_\pm^4 , F_1 , F_2 , and H . Figure 17(a) shows the global view of Γ . We observe Γ entering into the region of SAOs near the stable branch C_-^4 of C . The MMO spirals as it enters the scroll-like region of \mathcal{H} and makes a slow passage through the Hopf point H to S^2 . An enlargement of Γ 's entry into the scrolls of \mathcal{H} (red surface) and its slow passage through H are shown in inlay (b). In the enlargement, we also see Γ exit the region of SAOs by spiralling out of the scrolls of \mathcal{H} to the underside of the flatter region of \mathcal{H} . In the global view (a), we observe Γ subsequently tracking an orbit segment in this flatter area of \mathcal{H} . The MMO travels into the blue region of \mathcal{H} before following S^3 . Near F_1 , Γ falls off S^3 and makes a single LAO back to the attracting slow manifold near C_-^4 .

Figure 18 shows the isola (red and blue curve) of the MMO Γ over the time scaling parameter ε . The red segment of the isola indicates where Γ has at least one unstable Floquet multiplier and the blue segment indicates where Γ is stable. The green dot labeled (a) corresponds to the MMO shown in Figure 17 as well as Figure 18(a). Green dots labeled (b), and (c) refer to Figures 16(b) and 16(c), respectively. Only the green dot labeled (a), corresponding to the original value of epsilon, has an associated Γ that is stable. The Γ s associated with green dots labeled (b) and (c) correspond to Γ that have at least one unstable Floquet multiplier.

Figure 16 shows \mathcal{H}_0 (red-blue fade surface) and several objects of system (2) with the full system MMO Γ in projection onto (B, A, X) -space. Panels (a), (b), and (c) respectively show Γ for values of ε corresponding to green dots labeled (a), (b), and (c) in Figure 18. Also shown are segments of C^3 , C^2 , and C_-^4 with F_1 and H . A jump back trajectory \mathcal{J} (magenta curve) connects F_1 to the equilibrium of (2) in C_-^4 corresponding to $B = F_{1B}$. The jump back trajectory's dual $\mathcal{J}^* \in \mathcal{H}_0$ (magenta curve) lies on the other side of and at an equal distance away from H . A surface of singular POs \mathcal{P} (midnight grape surface) for varying ε forms a cone that originates from H and terminates in a homoclinic connection of a saddle of (2) in C^3 . Panel (a) shows Γ for the original value of $\varepsilon = 0.0037$. The LAO after Γ passes F_1 can be seen tracking \mathcal{J} into the region of SAOs. We can easily see the passage of Γ through the Hopf point H , compare with Figure 15. As Γ passes through H , we observe it spiralling through the interior of \mathcal{P} . The MMO's exit out of the region of LAOs occurs near \mathcal{J}^* . Drift in the B -direction causes Γ to distances itself from \mathcal{J}^* on its way to C^3 . Panel (b) shows Γ for $\varepsilon = 0.0005$. The MMO makes an LAO to the region of SAOs via the homoclinic connection at the widest end of \mathcal{P} . The SAOs of Γ track \mathcal{P} , but do not pass through H . Rather, Γ leaves C_-^4 before reaching C^3 , passing through \mathcal{P} in the (B, A, X) -projection. When Γ is away from C , we see less drift of Γ in the B -direction due to the smaller value of ε , compare with panel (a). Panel (c) shows Γ for $\varepsilon = 0.0038$ which has two LAOs. For this value of ε , Γ enters and exits the region of SAOs near \mathcal{J} and \mathcal{J}^* respectively. An early LAO back to C^2 occurs between exit and reentry into the region of SAOs.

An animation of the change in Γ 's geometry for varying ε can be found in the supplementary materials. In this animation, we see the Γ shown in Figure 16(a) morphing smoothly into the Γ shown in Figure 16(b). We then see Γ shown in Figure 16(b) morphing into the Γ shown in Figure 16(c). Finally, we see Γ shown in Figure 16(c) morph back into Γ shown in Figure 16(a). The green dot shown in the inlay tracks the location of Γ around the isola from figure 14.

References

- Benoît, E. [1982] “Systèmes lents-rapides dans \mathbb{R}^3 et leurs canards,” *Proceedings of the Third Schnepfenried Geometry Conference* **2**, 159–191.
- Benoît, E. [1985] “Enlacements de canards,” *Comptes Rendus Mathematique Academie des Sciences* **300**, 225–230.
- Benoît, E., Callot, J. F., Diener, F. & Diener, M. [1981] “Chasse au canard,” *Collectanea Mathematica* **31**, 37–119.
- Brøns, M. & Bar-Eli, K. [1991] “Canard explosion and excitation in a model of the Belousov-Zhabotinskii reaction,” *Journal of Physical Chemistry A* **95**, 8706–8713.
- Brøns, M., Krupa, M. & Wechselberger, M. [2006] “Mixed mode oscillations due to the generalized canard phenomenon,” *Fields Institute Communications* , 39–63.
- De Maesschalck, P. & Wechselberger, M. [2015] “Neural Excitability and Singular Bifurcations.” *The Journal of Mathematical Neuroscience* **5**.
- Desroches, M., Guckenheimer, J., Krauskopf, B., Kuehn, C., Osinga, H. & Wechselberger, M. [2012] “Mixed-Mode Oscillations with Multiple Time Scales.” *SIAM Review* **54**, 211–288.
- DesRoches, M., Krauskopf, B. & Osinga, H. [2009] *Elements of Applied Bifurcation Theory*, 2nd ed. (Springer International Publishing).
- Desroches, M., Krauskopf, B. & Osinga, H. [2009] “The geometry of mixed-mode oscillations in the Olsen model for peroxidase-oxidase reaction.” *Discrete & Continuous Dynamical Systems* **2**, 807–827.
- Doedel, E. [2007] *AUTO-07p: Continuation and Bifurcation Software for Ordinary Differential Equations*, URL <http://indy.cs.concordia.ca/auto/>, with major contributions from A.R. Champneys, F. Dercole, T.F. Fairgrieve, Y.A. Kuznetsov, R.C. Paffenroth, B. Sandstede, X. Wang and C. Zhang.
- Farjami, S., Kirk, V. & Osinga, H. [2018] “Computing the Stable Manifold of a Saddle Slow Manifold.” *SIAM Journal on Applied Dynamical Systems* **17**, 350–379.
- Fenichel, N. [1979] “Geometric singular perturbation theory for ordinary differential equations,” *Journal of Differential Equations* **31**, 53–98.
- FitzHugh, R. [1955] “Mathematical models of threshold phenomena in the nerve membrane,” *The bulletin of mathematical biophysics* **17**, 257–278.
- Guckenheimer, J. [1985] “Singular hopf bifurcation in systems with two slow variables,” *SIAM Journal on Applied Dynamical Systems* **7**, 1355–1377.
- Háro, A. & de la Liave, R. [2006] “A parameterization method for the computation of invariant tori and their whiskers in quasi-periodic maps: Rigorous results,” *Journal of Differential Equations* **228**, 530–579.
- Harvey, E., Kirk, V., Osinga, H., Sneyd, J. & Wechselberger, M. [2010] “Understanding anomalous delays in a model of intracellular calcium dynamics,” *Chaos: An Interdisciplinary Journal of Nonlinear Science* **20**.
- Hasan, C., Krauskopf, B. & Osinga, H. [2018] “Saddle slow manifolds and canard orbits in \mathbb{R}^4 and application to the full Hodgkin-Huxley model,” *Journal of Mathematical Neuroscience* **8**.
- Hudson, J. L., Hart, M. & Marinko, D. [1979] “An experimental study of multiple peak periodic and nonperiodic oscillations in the Belousov-Zhabotinskii reaction,” *The Journal of Chemical Physics* **71**, 1601–1606.
- Jorba, A. & Olmedo, E. [2009] “On the computation of reducible invariant tori on a parallel computer,” *SIAM Journal on Applied Mathematics* **8**, 1382–1404.
- Krauskopf, B., Osinga, H. & Galán-Vioque [2007] *Numerical continuation methods for dynamical systems* (Springer International Publishing).
- Krauskopf, B. & Rieß, T. [2008] “A lin’s method approach to finding and continuing heteroclinic connections involving periodic orbits,” *Nonlinearity* **21**, 1655–1690.
- Krupa, M., Popović, N. & Kopell, N. [2008] “Mixed-mode oscillations in three time-scale systems: A prototypical example,” *SIAM Journal on Applied Dynamical Systems* , 361–420.
- Kuehn, C. & Szmolyan, P. [2015] “Multiscale Geometry of the Olsen Model and Non-classical Relaxation Oscillations.” *Journal of Nonlinear Science* **25**, 583–629.

- Kuznetsov, Y. A. [2009] *Elements of Applied Bifurcation Theory*, 2nd ed. (Springer International Publishing).
- Lin, X. [1989] “Shadowing lemma and singularly perturbed boundary value problems,” *SIAM Journal of Applied Mathematics* **49**, 26–54.
- Mitry, J., McCarthy, M., Kopell, N. & Wechselberger, M. [2013] “Excitable neurons, firing threshold manifolds and canards,” *The journal of mathematical neuroscience* **3**.
- Olsen, L. [1983] “An enzyme reaction with a strange attractor.” *Physics Letters A* **94**, 454–457.
- Otto, C., Ludge, K., Vladimirov, A. G., Wolfrum, M. & Scholl, E. [2012] “Delay-induced dynamics and jitter reduction of passively mode-locked semiconductor lasers subject to optical feedback,” *New Journal of Physics* **14**.
- Piltz, S. H., Veerman, F., Maini, P. K. & Porter, M. A. [2017] “A predator–2 prey fast–slow dynamical system for rapid predator evolution,” *SIAM Journal on Applied Dynamical Systems* **16**, 54–90.
- Rockafellar, R. T. & Wets, R. J.-B. [2009] *Variational Analysis*, 3rd ed. (Springer International Publishing).
- Van der Pol, B. [1927] “Forced oscillations in a circuit with non-linear resistance. (Reception with reactive triode).” *The London, Edinburgh, and Dublin Philosophical Magazine and Journal of Science* **3**, 65–80.
- Vo, T., Bertram, R. & Wechselberger, M. [2013a] “Multiple geometric viewpoints of mixed mode dynamics associated with pseudo-plateau bursting,” *SIAM Journal on Applied Dynamical Systems* **12**.
- Vo, T., Tabak, J., Bertram, R. & Wechselberger, M. [2013b] “A geometric understanding of how fast activating potassium channels promote bursting in pituitary cells,” *Journal of Computational Neuroscience* **36**.
- Waalkens, H., Burbanks, A. & Wiggins, S. [2005] “A formula to compute the microcanonical volume of reactive initial conditions in transition state theory,” *Journal of Physics A: Mathematical and General* **38**, L759–L768, URL <http://stacks.iop.org/0305-4470/38/i=45/a=L03>.
- Zhang, W., Krauskopf, B. & Kirk, V. [2012] “How to find a codimension-one heteroclinic cycle between two periodic orbits,” *Discrete and Continuous Dynamical Systems* **32**, 2825–2851.